DESIGN OF AN ULTRA-WIDEBAND SPIRAL ANTENNA FOR GROUND-PENETRATING MICROWAVE IMPULSE RADAR APPLICATIONS

A Thesis

presented to

the Faculty of California Polytechnic State University,

San Luis Obispo

In Partial Fulfillment

of the Requirements for the Degree

Master of Science in Electrical Engineering

by

Bradley Curtis Hutchinson

June 2015

© 2015
Bradley Curtis Hutchinson
ALL RIGHTS RESERVED

COMMITTEE MEMBERSHIP

TITLE:	Design of an Ultra-Wideband Spiral Antenna for Ground-Penetrating Microwave Impulse Radar Applications
AUTHOR:	Bradley Curtis Hutchinson
DATE SUBMITTED:	June 2015
COMMITTEE CHAIR:	Dennis Derickson, Ph.D. Department Chair and Associate Professor of Electrical Engineering
COMMITTEE MEMBER:	Dean Arakaki, Ph.D. Associate Professor of Electrical Engineering
COMMITTEE MEMBER:	Xiaomin Jin, Ph.D. Professor of Electrical Engineering

ABSTRACT

Design of an Ultra-Wideband Spiral Antenna for Ground-Penetrating Microwave Impulse Radar Applications

Bradley Hutchinson

Radar systems that allow early detection of underground IEDs can save lives. The Microwave Impulse Radar (MIR) capable of IED detection requires antennas capable of transmitting sub-nanosecond pulses over ultra-wideband (UWB) frequency ranges. This thesis investigates the suitability of a novel MIR antenna for high-accuracy ground-penetrating radar (GPR) applications. Key GPR antenna considerations are pulse dispersion, size, and cost. UWB horn antennas provide excellent dispersion performance but limit system efficacy due to significant size and cost requirements. Micro-strip spiral antennas provide a low-cost alternative to UWB horn antennas, but common spiral designs demonstrate poor pulse dispersion performance. The article “Low-Dispersion Spiral Antennas” proposes using combination spirals, which combine the performance of multiple simple spiral antennas. This work investigates combination spiral suitability through 3D EM simulations and micro-strip fabrication. Testing results indicate that combination spirals possess improved pulse fidelity versus current spiral designs. Size and cost improvements are realized over horn antenna solutions. Updated simulation hardware and fabrication equipment could allow future combination spiral antennas to rival horn antenna performance.

ACKNOWLEDGMENTS

Firstly, I would like emphasize that none of this would have been possible without the intellectual and financial support of the Lawrence Livermore National Laboratories.

Between my time at Cal Poly and at LLNL, the list of individuals who have made a positive impact on me and on this thesis is far too long to give them each the thanks that they deserve. However, here are a select few who I believe deserve special recognition:

Bruce Henderer, who, by selecting and guiding me, has changed the path of my career and my life, for which I will be forever grateful.

Jae Jeon, my exceedingly patient mentor, who spent six long months working overtime and suffering constant interruptions in order to make sure I succeeded. Thank you for answering all the questions an inquisitive newcomer to the RF field could possibly ask.

Dr. Dennis Derickson, who, as department chair and professor, found the time to be my advisor and provide substantial written feedback despite having no personal investment in the project.

TABLE OF CONTENTS

Page

LIST OF TABLES

LIST OF FIGURES

1. INTRODUCTION

1.1 Microwave Impulse Radar (MIR)

Microwave impulse radar, also known as ultra-wideband (UWB) radar, is an electromagnetic imaging and detection technology. MIR operates by radiating very short time-domain RF impulses at a target and analyzing returns [1]. MIR differs from conventional microwave radar systems that use bursts of single-frequency energy, or more advanced systems that step through multiple frequencies.

In order to achieve optimum radar performance, it is important that MIR antennas output a minimum duration time-domain pulse, necessitating antennas that can radiate all frequencies across a wide band. The relationship between short time-domain pulses and ultra-wideband frequency domain content is defined in Equation 1, the Fourier Transform definition. G(f) is the frequency spectral content of the time domain function g(t), f is frequency in Hz and t is time in seconds.

$$G(f) = \int_{-\infty}^{\infty} g(t) e^{-2\pi i f t} dt \qquad (1)$$

An ideal infinitesimal-time impulse g(t) = δ(t) Fourier transforms to a constant, where |G(f)| is independent of

frequency. Therefore narrow time domain pulses have wide frequency domain content.

Radar systems use Equation 2, the relationship between time t, distance d, and velocity of electromagnetic wave propagation v_p, to convert time differences between transmitted and received energy into absolute distances.

$$d = v_p * t \tag{2}$$

Assuming a constant velocity of propagation, distance is directly proportional to time. Short time-domain pulses therefore lead to high spatial resolution by resolving return pulses that are spatially similar (and thus close in time as seen in the relationship from Equation 2) caused by reflections from objects at similar distances from the radar. An in-depth explanation of this relationship is shown in Section 1.2.2.

An example block diagram of an MIR system is shown in Figure 1. The impulse generator, synchronized with a reference oscillator, must produce a pulse of the required width. There are various methods to accomplish this, however impulse generator specifications are outside the scope of this project. Assuming the impulse generator is capable, the system bottleneck is the transmit and receive antennas. Each antenna must transform short-

time electrical pulses into radiated energy without changing waveform characteristics.

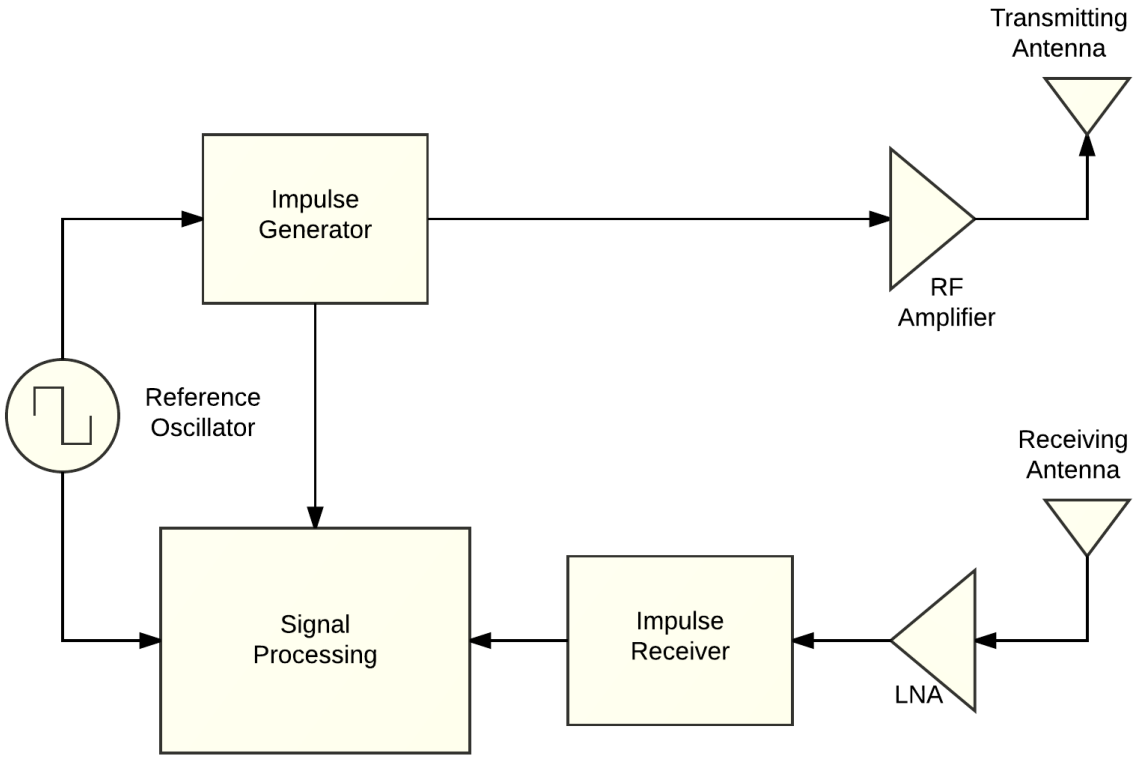

Figure 1: MIR system block diagram. Reference oscillator synchronizes all radar components. Impulse generator produces a short-time pulse synchronized with the oscillator, amplified, and applied to the transmitting antenna. The receive antenna captures reflected energy, which is amplified and sent to a receiver. All radar system data is applied the signal processing block for analysis and image creation.

1.2 Important Radar Antenna Properties

The three primary antenna parameters that affect short-time pulse transmission are return loss, group delay, and pulse fidelity. Antenna deficiencies in each area uniquely affect the pulse shape.

1.2.1 Return Loss

The return loss of a device measures incident energy absorption by a system. Energy absorption in an antenna is primarily due to radiation, therefore return loss characterizes an antenna's ability to transmit signals.

An effective ultra-wideband antenna transmits all pulse frequencies, which requires return loss less than -10 dB. A -10 dB maximum return loss corresponds to a minimum 90% of total incident power radiating into free space.

1.2.2 Group Delay

Any single-frequency signal passed through a radiating antenna will experience a time delay called group delay as a function of frequency, $g_d(f)$. Group delay is the negative frequency

derivative of phase φ, as shown in Equation 3, where ω is the frequency in radians per second.

$$g_d = -\frac{d\varphi}{d\omega} \tag{3}$$

A constant group delay versus frequency leads to a constant propagation time delay and an undistorted output signal. From Equation 2, a constant time delay τ adds a constant distance, C, to radar calculations.

$$t \rightarrow t + \tau$$

$$d = v_p * (t + \tau) = v_p * t + v_p * \tau$$

$$= v_p * t + C$$

C is a constant that is easily eliminated in software. The radar software evaluates the time delay of the return pulse, corrects for the known antenna group delay, and determines a single value for d, the antenna to target round-trip distance.

A variable group delay versus frequency causes a frequency dependent variation in time delay, τ(f). Equation 2 reveals that a frequency dependent time delay adds a frequency dependent distance, C(f), to radar calculations as shown in Equation 4.

$$t \rightarrow t + \tau(f)$$

$$d = v_p * (t + \tau(f)) = v_p * t + v_p * \tau(f)$$
$$= v_p * t + C(f) \quad (4)$$

Frequency variation of C(f) prevents radar software from determining a single value for d. Consider an ultra-wideband frequency range from f_1 to f_2. Evaluating Equation 4 at f_1 and f_2 returns the distances d_1 and d_2. Larger group delay variations between f_1 and f_2 lead to larger variations in C(f) and therefore a larger apparent discrepancy when determining range to target, between d_1 and d_2. Therefore radar distance resolution is directly influenced by antenna group delay performance.

The relationship between group delay and radar resolution can also be seen by analyzing the effect of a variable group delay on radiated pulse length. Figure 2 shows input and output waveforms of an example system with a variable group delay:

$$g_d(f) = A + C(f)$$

The constant portion of the group delay, A, causes a time delay, τ, between input and output pulses. The frequency-varying portion of the group delay, C(f), causes some input pulse frequency components to radiate later than others, causing the waveform to disperse in the time domain from width W_{in} to W_{out}. This is called pulse dispersion [2].

Figure 3 illustrates the effect of pulse dispersion upon a train of pulses. Impulse trains are produced at the receiving antenna when a radiated pulse reflects off of closely spaced objects. The three non-dispersed pulses are easily resolved as their amplitude decreases to zero before the subsequent pulses arrive. However, the dispersed pulses are wider than the time differences between returns, causing adjacent pulse overlap. This overlap prevents radar software from distinguishing between returns from closely spaced objects, decreasing system spatial resolution. Therefore any antenna used in an MIR system must be designed to minimize group delay variations over the radiating bandwidth.

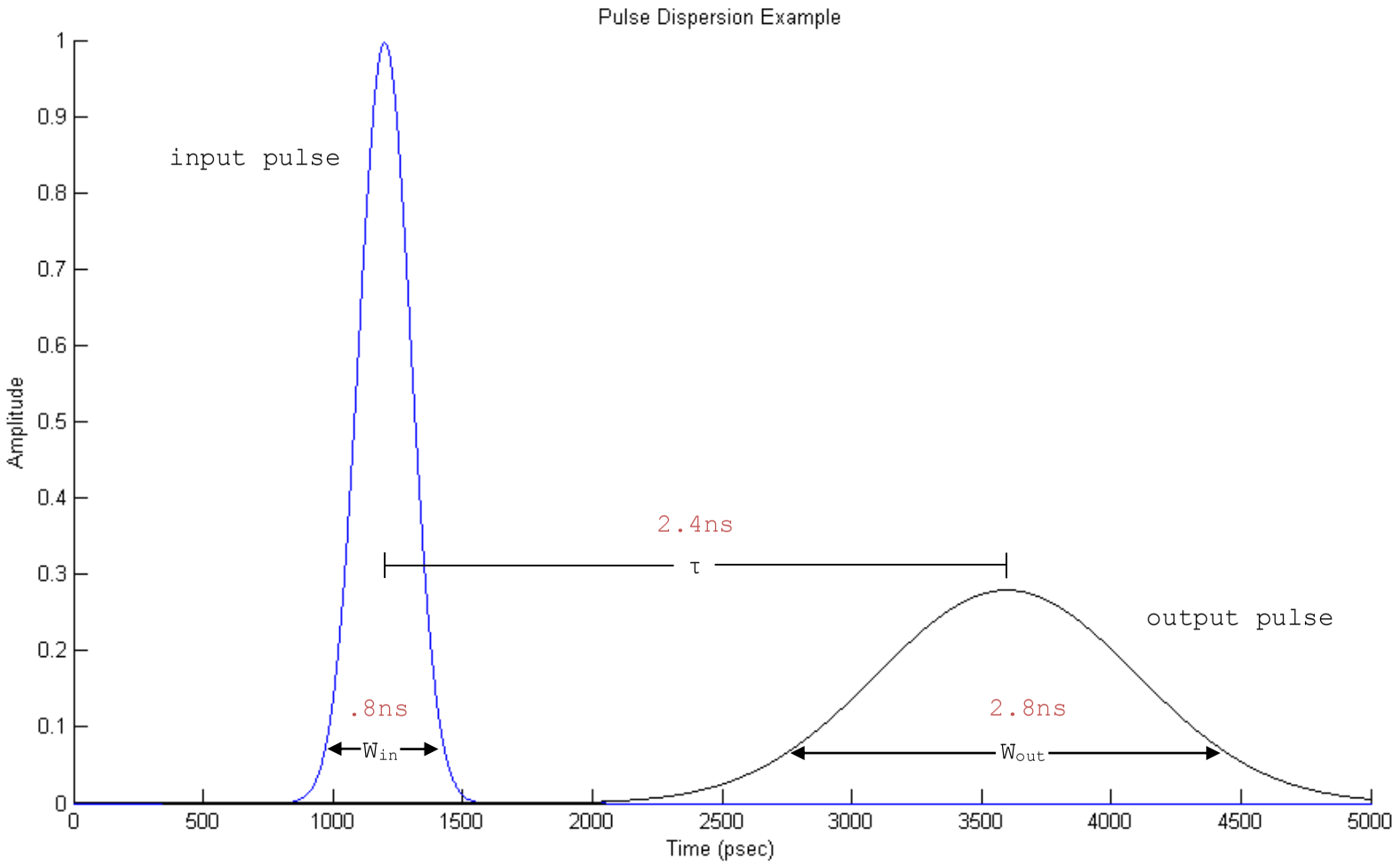

Figure 2: Input and output pulses of a non-ideal system with varying group delay versus frequency. Asynchronous radiation of the input pulse causes pulse dispersion, increasing pulse width by 2 ns.

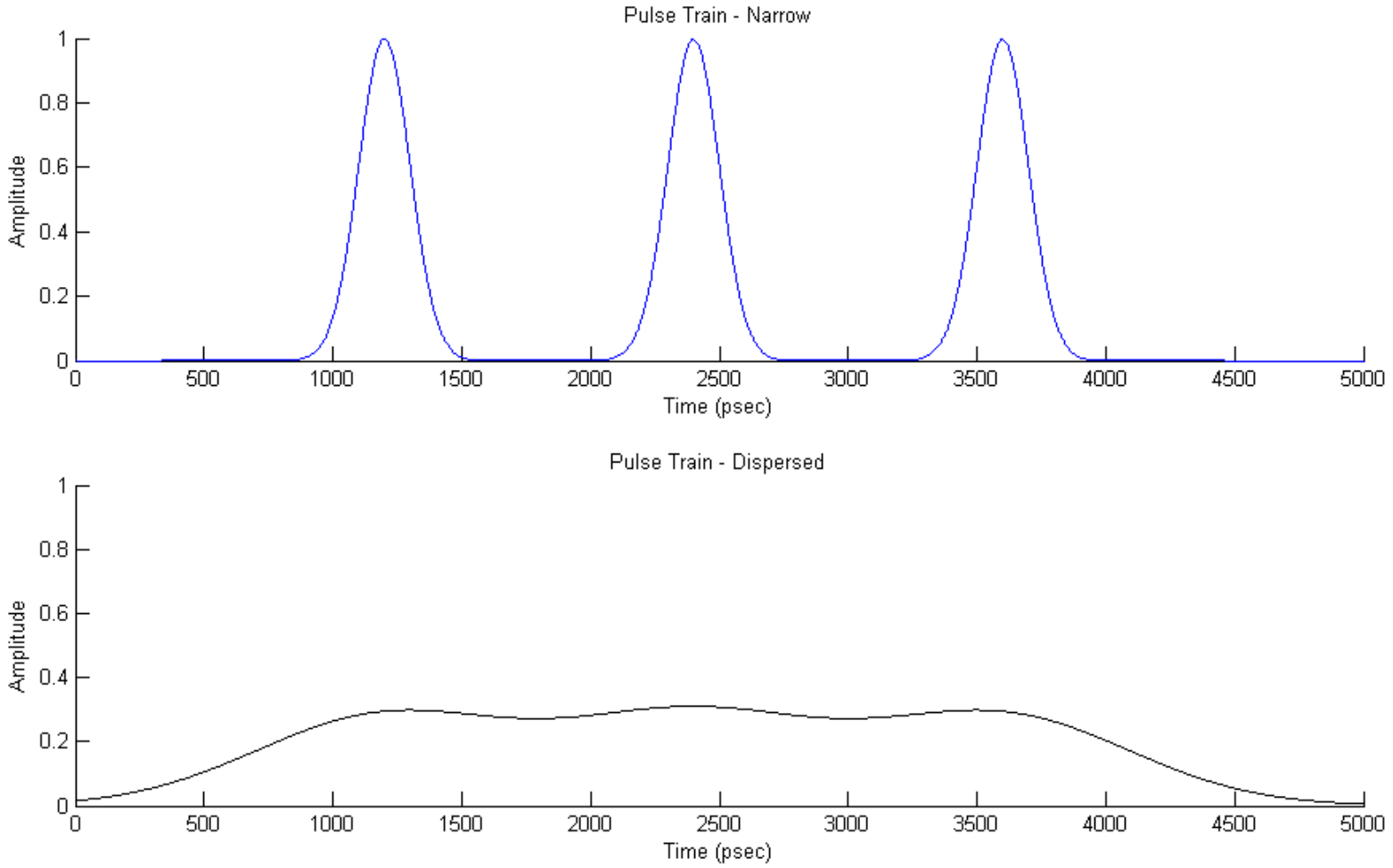

Figure 3: Pulse trains formed by radiated energy reflecting off of closely spaced objects. Top: Ideal pulse train assuming no dispersion. Individual pulses are easily differentiated as unique returns. Bottom: Dispersed pulse train due to non-ideal system. Overlapping pulses cannot be resolved into unique returns.

1.2.3 Pulse Fidelity

Pulse length is not the only signal trait that must be maintained by the antenna, and cannot be used as the sole metric for determining antenna performance. Pulse shape can also have an effect upon radar performance. Therefore an additional metric must be used to evaluate radar antennas, known as pulse fidelity F [3].

$$F = \max_{\tau} \left| \frac{\int_{-\infty}^{\infty} a(t) r(t+\tau) dt}{\sqrt{\left(\int_{-\infty}^{\infty} a(t)^2 dt\right)\left(\int_{-\infty}^{\infty} r(t)^2 dt\right)}} \right|, \; 0 \leq F \leq 1 \qquad (5)$$

Mathematically, pulse fidelity F is the maximum cross-correlation between the normalized output pulse a(t) and the reference input pulse r(t), as seen in Equation 5. The value of F is maximally equal to 1 when the input and output pulses are identical in shape. Parameter τ is used to time sweep r(t) during optimization of F, eliminating the effect of non-zero time delay between waveforms.

Figure 4 illustrates the pulse fidelity calculation graphically. Output waveform a(t) is scaled until the area under the a(t) and r(t) are equal. Sweeping τ shifts the reference input pulse r(t) until the area that resides beneath both curves is maximized.

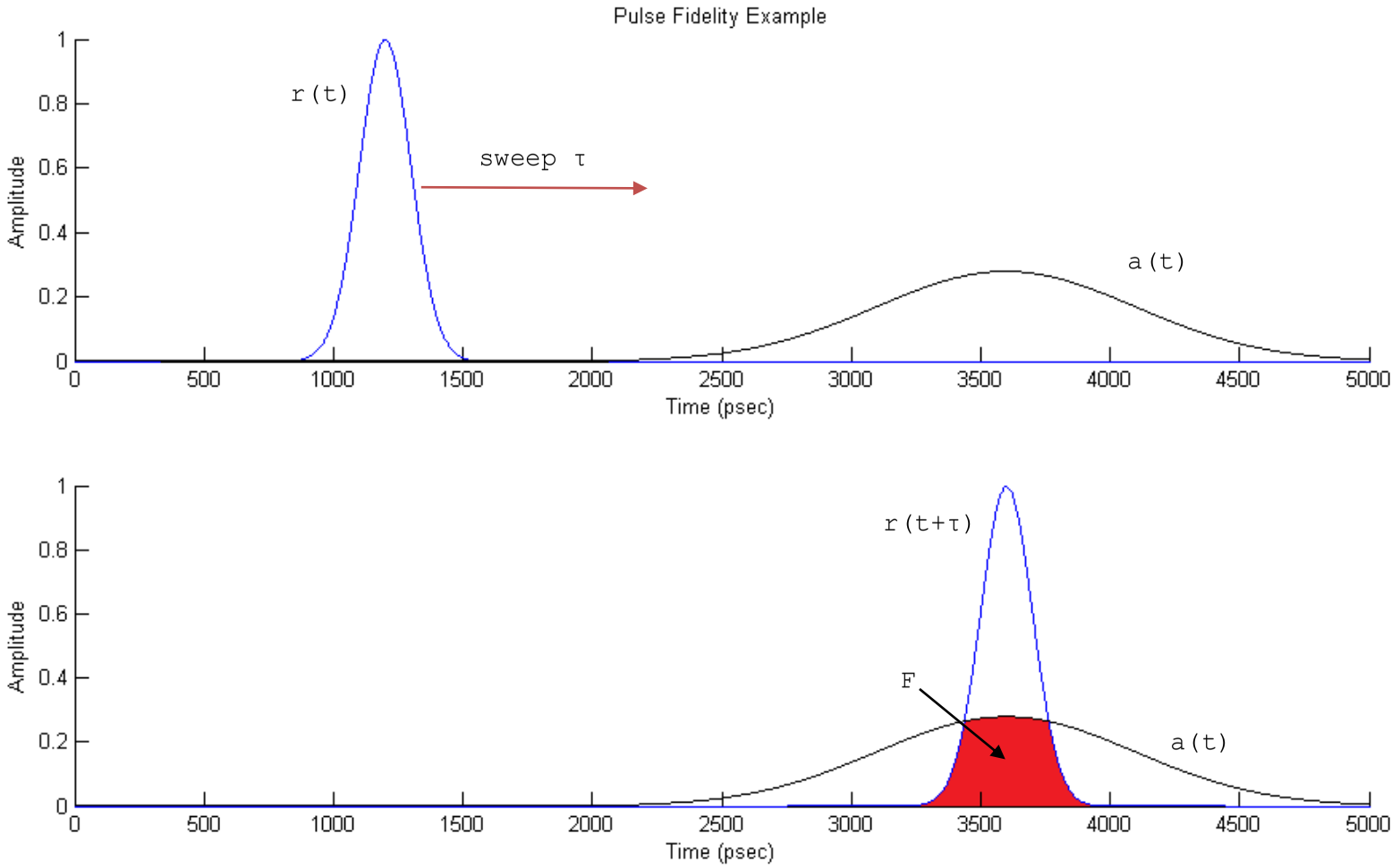

Figure 4: Top: Reference input pulse r(t) and time delayed, normalized output pulse a(t). Sweeping τ shifts r(t) until shared area F is maximized. Bottom: Pulse fidelity result F calculated as ratio between shared and total area beneath the curves

Finally, the resulting integral is normalized against the total area under the curve such that F is maximally equal to 1 when the input and output pulses are identical in shape.

1.2.4 Antenna Properties Summary

In summary, the return loss result will be used to evaluate the frequency range of the antenna, the group delay variation provides insight into the quantity of pulse dispersion, and the pulse fidelity quantifies the differences between input and output pulse shape. Therefore an antenna's ability to effectively radiate a short pulse is fully characterized through return loss, group delay, and pulse fidelity testing.

1.3 Ground-Penetrating Radar

The antenna designed in this project is intended for a ground-penetrating radar system mounted on the front of a vehicle, as shown in Figure 5. The system uses a linear array of antennas oriented to aim at the ground in front of the vehicle.

Figure 5: Top: 16-element ground-penetrating radar array. The antennas used in this example are hexagonal horn antennas. Bottom: Array mounted to an SUV for system testing.

The primary application of this radar system is ground-penetration imaging to detect buried objects, specifically improvised explosive devices (IEDs) [4]. From an antenna design perspective, the important term here is "improvised"; these devices can be almost any shape and size. In order to ensure strong radar returns from potentially narrow objects with unknown orientations antenna polarization must be considered. For example, an x-oriented linearly polarized antenna could potentially miss objects with small x-directional cross-sections relative to one wavelength. By utilizing antennas that are

circularly polarized with an axial ratio approaching 1, radar returns can be received regardless of target orientation.

1.4 Horn Antenna

The current optimum UWB antenna choice for impulse radar applications is the hexagonal horn with abrupt radiator shown in Figure 6 [5]. This UWB horn design operates from 0 GHz to above 12 GHz. It has inherently constant group delay versus frequency due to the abrupt radiator design, which causes all frequencies to radiate from the same location on the launcher plate. It also has very low cross-coupling due to the horn waveguide.

However, this antenna design is linearly polarized and has manufacturing issues that limit its potential in portable radar applications. Each horn must be soldered and manually tuned due to the complicated geometry of the launcher plate inset within the horn wall as identified in Figure 6. This raises costs while reducing repeatability and consistency between antennas.

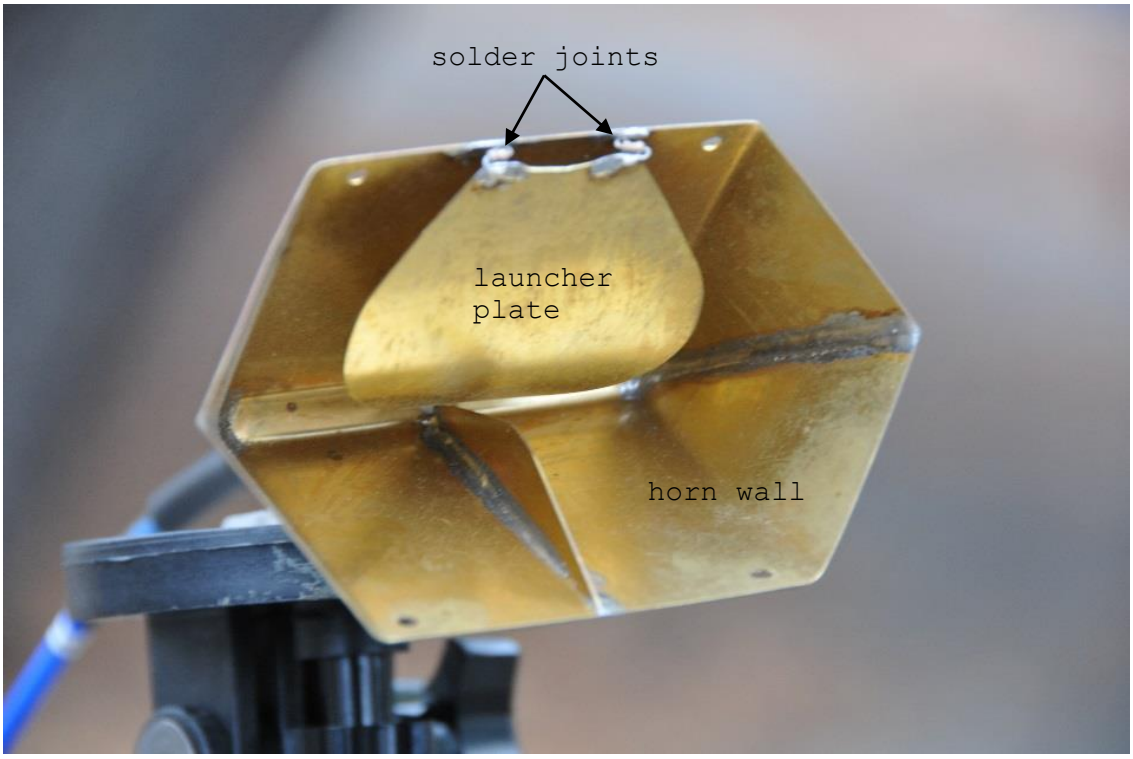

Figure 6: The hexagonal horn antenna with abrupt radiator that is currently used in the LLNL UWB radar system [5].

The design also requires discrete resistor components between the launcher plate and the horn wall, shown at the top of the horn in Figure 6. These solder joints are fragile, an issue of critical importance for a mobile radar intended for mounting on off-road vehicles for detection of lethal devices. Due to the 3D nature of horn antennas, the hexagonal horn requires more space than a planar design. The waveguide bulk limits potential portable applications of the antenna.

1.5 Spiral Antennas

An alternative for the horn antenna to limit size and cost is required. It must also be circularly polarized. In the short list of antenna types that are simultaneously UWB, circularly polarized, and machine-fabricable in a micro-strip environment, spiral antennas are a particularly valuable choice due to its frequency-independent (FI) properties. According to Rumsey [6], there is a class of antennas whose pattern and impedance are practically independent of frequency for all frequencies above a minimum cutoff value. The general formula for the shape of these FI antennas is

$$r = e^{\alpha(\varphi+\varphi_0)}F(\theta) \qquad (6)$$

where r, θ, and φ are spherical coordinates, α and φ_0 are constants, and F(θ) is any function of theta. For such devices a frequency change is equivalent to an antenna rotation about θ = 0.

The key significance of frequency independence on spiral antennas is that a change in frequency only rotates the active region, the radiating area, along the spiral arms. As long as the arm length is sufficient, any frequency can effectively radiate. Therefore the scaling factor, α, determines the spiral arm length and consequently the antenna's lower cutoff frequency, allowing for

FI antennas to be scaled in size according to the desired frequency response. By choosing a scaling factor large enough to achieve desired electrical performance but small enough to improve upon the hexagonal horn size, it should be possible to create a design that rivals or exceeds the performance of existing designs at a lower cost.

The primary issue preventing frequency independent antennas from use in MIR systems is pulse dispersion. Because the active region moves as a function of frequency, FI antennas radiate dispersed signals [2].

1.6 Prior Work

A possible solution to the compromised pulse fidelity response of spiral antennas is to use a novel spiral geometry [7]. Certain spiral antenna equations are shown to inherently possess a constant group delay at frequencies above cutoff. The proposed spiral is closely related to the Archimedean spiral shown in Figure 7, a common and well analyzed antenna design.

The Archimedean spiral is one of a class of spirals including the Fermat's spiral (parabolic spiral) and hyperbolic spiral. The general equation for these spirals in spherical coordinates is

$$r = a\varphi^{1/n} \quad (7)$$

When n = 1, the resulting spiral is known as an Archimedean spiral, where arm width and spacing remains constant as arm length increases. An example of a single Archimedean spiral arm is shown in Figure 7. When n = 2, the resulting spiral is known as a Fermat spiral. The primary feature of the Fermat spiral is that arm spacing decreases as a function of radius or arm length. Figure 8 shows an example of a 2 arm Fermat spiral.

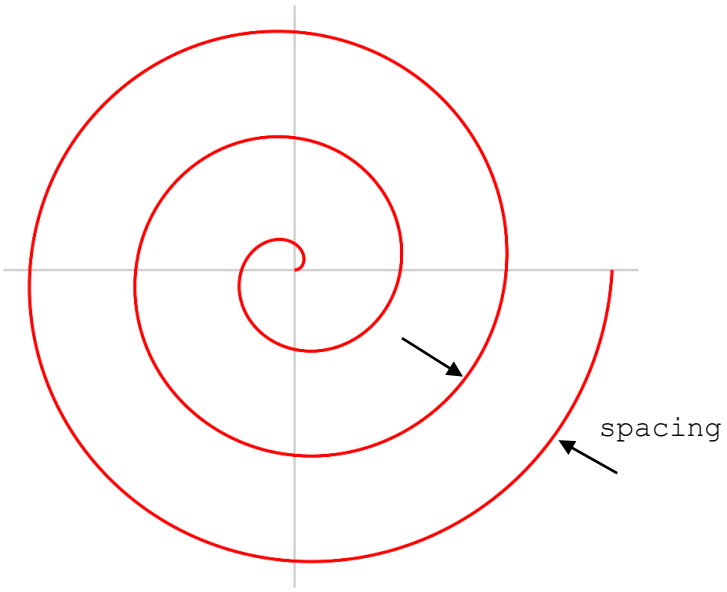

Figure 7: Single Archimedean spiral arm. Arm spacing is constant as number of turns increases.

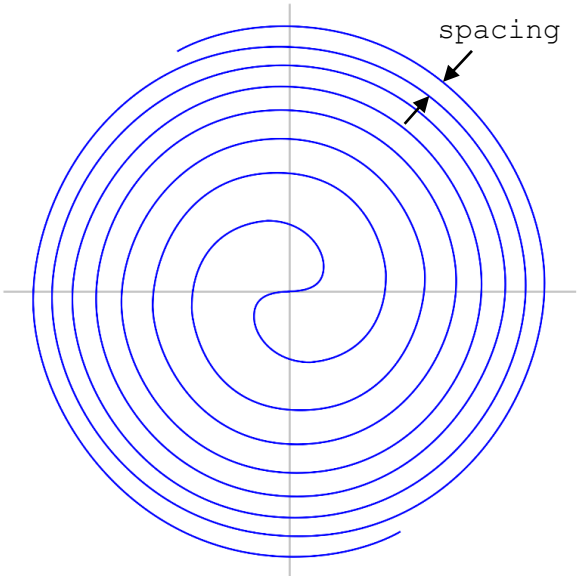

Figure 8: Two-arm Fermat spiral. Two arms are drawn to better illustrate the decreasing arm spacing with increasing number of turns.

As n increases, this spacing reduction becomes more pronounced. The author of the original article defines this class of shapes as power spirals.

The group delay of any spiral antenna is related to the feed-to-active region time delay [8]. The active region is the antenna section which radiates the input signal as electromagnetic waves [9]. This is calculated as

$$g_d = \frac{l(f)}{v_p} \tag{8}$$

where v_p is the travelling wave current phase velocity and l(f) is the unwrapped length of a spiral arm from feed point to active region. Computation of g_d for power spirals is as follows [7]:

$$l(\varphi) = \int_{\varphi_{feed}}^{\varphi_{active}} a\varphi^{1/n}$$

$$\partial\varphi = \frac{na}{n+1}\left[\varphi^{(n+1)/n}\right]\Big|_{\varphi_{feed}}^{\varphi_{active}}$$

$$= \frac{na}{n+1}\left[\left(\left(\frac{r(\varphi)}{a}\right)^{n}\right)^{(n+1)/n} - \left(\left(\frac{r_{in}}{a}\right)^{n}\right)^{(n+1)/n}\right]$$

$$l(\varphi) = \frac{n}{(n+1)a^{n}}\left[(r(\varphi_{active}))^{n+1} - (r_{in})^{n+1}\right]$$

$$r(\varphi_{active}) = \frac{\lambda}{2\pi} = \frac{v_p}{2\pi f}$$

Therefore total path length at a given frequency f is

$$l(f) = \frac{n}{(n+1)a^{n}}\left[\left(\frac{v_p}{2\pi f}\right)^{n+1} - (r_{in})^{n+1}\right]$$

Finally, group delay can be obtained from (8) as

$$g_d(f) = \frac{n}{(n+1)v_p a^{n}}\left[\left(\frac{v_p}{2\pi f}\right)^{n+1} - (r_{in})^{n+1}\right]$$

$$g_d(f) \propto \left(\frac{A}{f^{n+1}} + B\right) \qquad (9)$$

where A and B are constants.

This result indicates that the group delay is inversely proportional to f^{n+1}, where n is power spiral order. As shown in Figure 9, increasing n increases group delay slope vs frequency below cutoff and decreases slope above cutoff. By designing for an antenna cutoff frequency below the radiated pulse's cutoff, high n spirals should provide a constant group delay over the frequency band of interest.

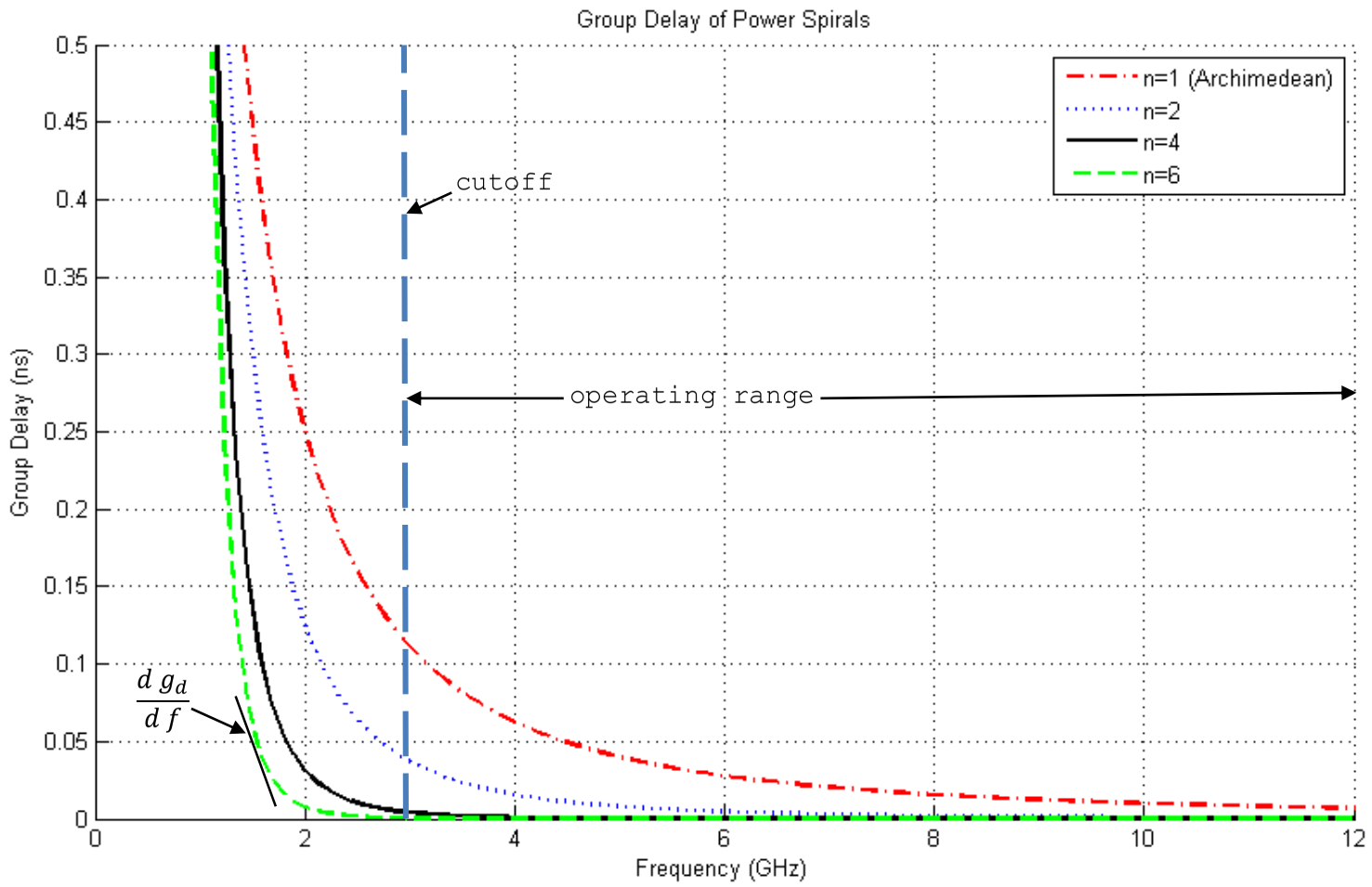

Figure 9: Theoretical group delay of the power spiral class of antennas from Equation 9. The change in group delay over the 3-12 GHz frequency range is minimized as n increases.

In order to generate antennas from these design equations, φ rotations of 90^0 are used to offset four identical spiral arms, which become the edges of two antenna arms. Figure 10 shows the 4-turn Archimedean spiral and 4-turn n = 2, 4, and 6 power spirals. Increasing n tightens the spiral wrap on the outer edges, corresponding to the low frequency active regions.

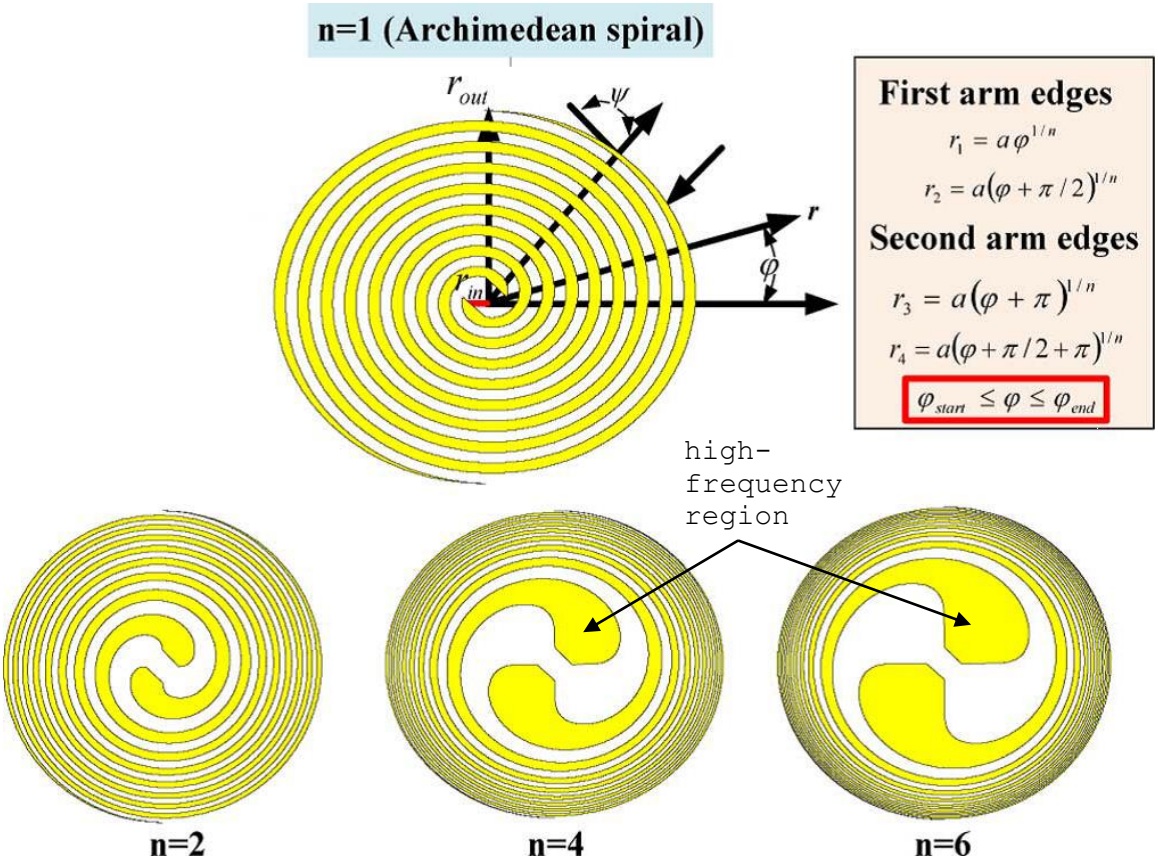

Figure 10: Power spirals with n = [1, 2, 4, 6]. Turn #1 of each spiral widens as n increases, introducing high frequency axial ratio degradation.

However, higher values of n also widen the first spiral turn. At very high frequencies, the active radiation region [9] exists entirely within the large center section of high n spirals, resulting in a radiation response similar to a micro-strip dipole as opposed to a spiral, reducing circular polarization at high frequencies. The paper proposes a solution to this issue by replacing the high frequency region of the antenna with an n = 1 Archimedean spiral, effectively combining the low frequency group delay performance of the power spiral with the high frequency axial ratio of an Archimedean spiral [10]. The spiral design replaces the first few turns of a power spiral with an Archimedean spiral; a combined spiral. An example combined spiral is shown in Figure 11. The effect of this alteration on group delay performance should be minimal according to Figure 9 given that all spirals achieve a flat group delay response at high frequencies.

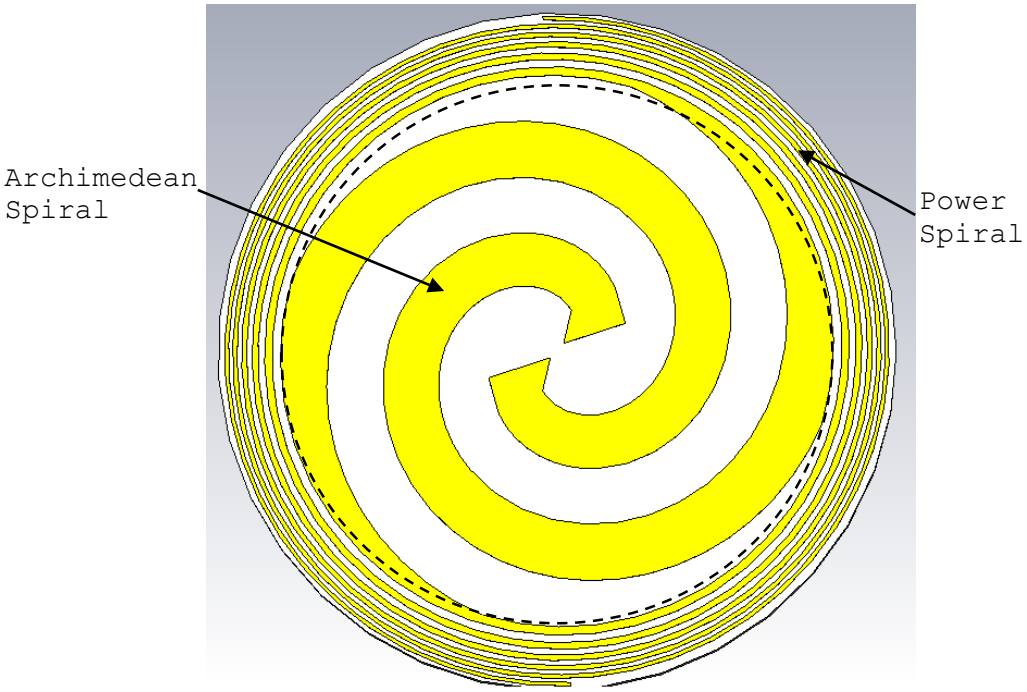

Figure 11: An example combined spiral. The dashed line defines the boundary between the inner Archimedean spiral (n=1) and the outer power spiral (n=6).

2. GOALS, REQUIREMENTS, AND SPECIFICATIONS

2.1 Goals

The assigned project tasks include:

- Confirm proposed combined spiral operation using EM simulation software, focusing on group delay performance.
- Adapt the combined spiral for frequency range of interest using frequency independence principles.
- Optimize the combined spiral group delay, axial ratio, and pulse fidelity.
- Fabricate and test a prototype to confirm simulation results and compare to three alternative designs: a hexagonal horn, planar horn, and simple Archimedean antenna.

2.2 Requirements

Low Profile	The antenna should be planar and use substrate no thicker than 1mm.
Low Cost	The antenna should be fabricable in a micro-strip environment.
High Performance	Antenna pulse fidelity should exceed Archimedean spiral performance with equivalent cutoff frequency.

Table 1: Design requirements. Size and cost compared to the existing horn antenna solution should be significantly improved, while electrical performance need only improve upon other planar designs. Archimedean pulse fidelity performance will be evaluated.

2.3 Antenna Specifications

3 dB Cutoff Frequency	800 MHz
Passband Return Loss	< -10 dB
Pulse Fidelity	> 0.5
Group Delay Variation above Cutoff	< 0.5 ns
Gain	5 dB

Table 2: Antenna design specifications. Cutoff and passband return loss specifications defined by radar system specifications. Group delay specification derived from theory, Equation 9. Gain specification based on spiral antenna theory [11].

3. DESIGN

In order to adapt the combination spiral antenna for ground-penetrating radar, it is necessary to first confirm existing results from the Low Dispersion Spiral Antenna paper [7]. Time and cost are both limiting factors to the number of fabricated prototypes, therefore a majority of design work will be done using a 3D electromagnetic solver.

There are several available EM solving software packages with the capabilities to properly design the combined spiral in 3D and evaluate antenna performance. CST Microwave Studio is chosen due to the availability of licenses and its intuitive parameter-based 3D modeling environment. Figure 12 shows the parameterized combined spiral model in CST. By designing the combined spiral using equation-defined shapes, parametric sweeps can be performed to optimize antenna performance.

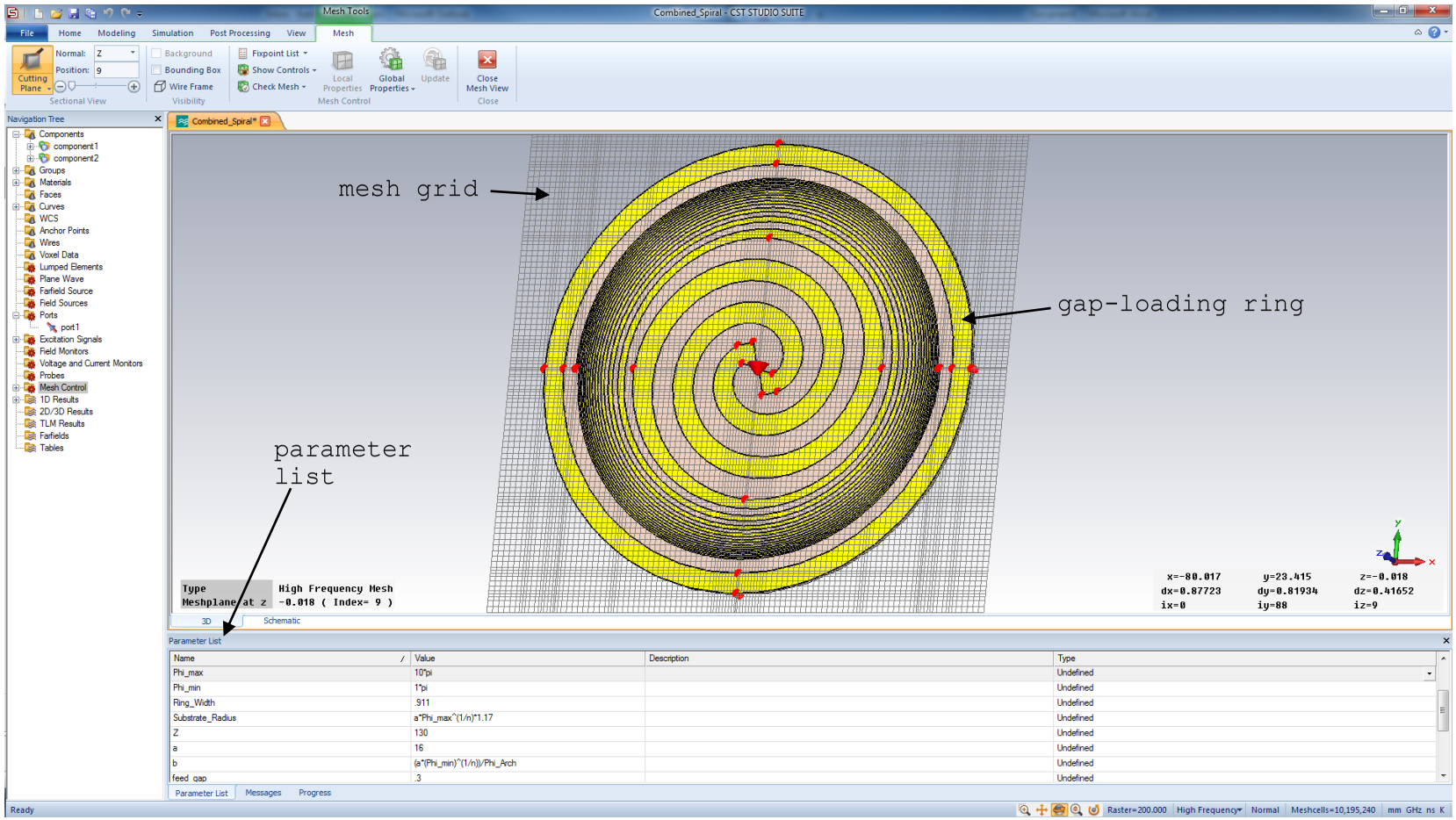

Figure 12: Parameterized combined spiral model in the CST Microwave Studio environment. Features of interest are the Cartesian mesh grid, gap-loading ring, and parameter list. The purposes of the mesh grid and gap-loading ring are explained in section 3.6 and 3.7 respectively.

3.1 Confirmation of Combined Spiral Operation

The antenna that must be recreated and tested to confirm the results of [7] is a 3GHz cutoff frequency design which combines an n = 6, N = 4 power spiral with an N = 1.2 Archimedean spiral merged at a radius r = 10mm. Recall that n is the power spiral order and N is the number of spiral turns.

The substrate chosen for all spiral designs is Rogers RT5880 [12]. It has a thickness of .79 mm and a dielectric constant of 2.2. RT5880 was chosen for its combination of relatively low dielectric constant, availability, and narrow thickness.

3.2 Designing for UWB Radar Applications

In order to utilize the entire available bandwidth of the UWB radar system, the antenna must operate at a frequency lower than the 3GHz specified in the existing design. The ground-penetrating radar specifications call for a cutoff of 800MHz. According to the frequency independence principles outlined in Section 1.5, a low cutoff could be accomplished simply by increasing the scale factor α of the existing antenna until an 800MHz cutoff is reached, however this would result in an antenna that exceeds volume restrictions according to design requirements. Recall the

characteristic equation for Archimedean and power spirals, Equation 7:

$$r = a\varphi^{1/n}$$

The parameterized model allows individualized control of the power and Archimedean spiral sections. Increasing scale (α) or number of turns (N) per section increases the total unwrapped length of each arm, decreasing cutoff frequency but simultaneously increasing antenna size, especially on the Archimedean section. Increasing the number of power spirals turns relative to the number of Archimedean spiral turns increases unwrapped arm length without increasing size but risks compromising the circular polarization performance. Finally, power spiral order (n) can be increased. This dramatically increases the unwrapped arm length for a given antenna size but significantly reduces the feature size of the outermost turns as shown in Figure 13, causing issues both in simulation time and fabrication accuracy. The largest cutoff frequency variations occur when varying power spiral parameters N and n.

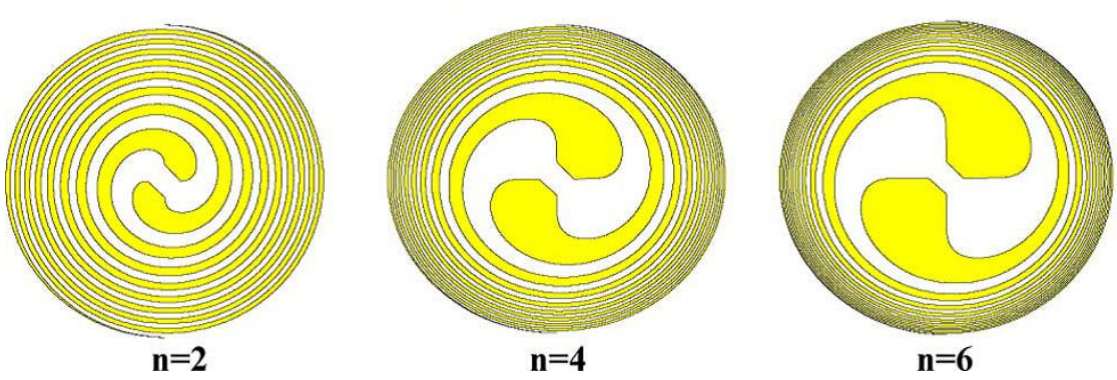

Figure 13: Feature size reduction of the outermost spiral turns as order (n) is increased. Resolution of available fabrication equipment limits the smallest arm width to 0.2mm.

The primary factor limiting design choices for number of turns (N) and order (n) of the power spiral is the 0.2mm LPKF S100 fabrication machine tolerance [13]. As each parameter increases, the outermost edge spiral arm width decreases. Therefore minimum spiral arm width must remain greater than the minimum fabrication tolerance, preferably at least twice as large to prevent milling defects and maintain uniformity between prototypes.

3.3 RAM Requirements

The CST frequency domain solver is used to evaluate spiral performance. The frequency solver utilizes a Cartesian mesh-grid which divides the structure's near-field region into a mesh of cells with Maxwell's equation individually solved in each cell.

The computer provided by LLNL for simulations utilizes an Intel i7 quad-core processor and 16GB of RAM. Quantity of RAM is particularly important in 3D EM simulations. It determines the upper limit on the number of mesh cells CST can process in a single run without crashing. However, due to the small feature size of the combined spiral along every axis, a standard x-by-y-by-z mesh grid configuration with sufficiently high resolution leads to upward of 300 million cells. Through trial and error, the maximum number of cells processed with 16GB of RAM was determined to be approximately 30 million cells. Adjustments are required to reduce the number of mesh cells by an order of magnitude while accurately resolving the structure.

3.4 Choosing Cutoff Frequency

Due to frequency independence properties, the spiral's low cutoff frequency can be reduced by increasing the scale factor while holding all other parameters constant. Design specifications call for a low frequency cutoff of 800 MHz, however this results in a CST model that greatly exceeds the 30 million mesh cell upper limit set by available hardware. Mesh cells in the z-direction must remain constant to accurately resolve the substrate and copper cladding. As the scale factor increases, mesh cell size in the x and y directions can also increase, but only to an upper

limit set by the lowest wavelength (highest frequency) of interest [14]. The UWB spirals must be confirmed at high frequencies, preferably up to 15GHz, however 12GHz is chosen to reduce this effect. Performance above 12GHz must be inferred.

The 800MHz design was attempted with reduced mesh cell size however results were unexpected; the low-density mesh size did not resolve the small design features. A 1.5GHz spiral is adequate for confirming combined spiral operation considering hardware limitations.

By increasing the cutoff frequency by a factor of 2, spiral dimensions in the x and y direction were halved, resulting in an overall mesh cell reduction by a factor of 4. Initial simulations of this adapted design result in a mesh grid requirement of approximately 90 million cells, 300% of the maximum allowed by the available hardware.

3.5 Adaptive Meshing

CST is capable of reducing total mesh cells through adaptive meshing. Adding supplemental processes and simulation time at the beginning of each run, the program analyzes the structure to identify high gradient value structures and reduces mesh cell sizes only in those areas. The program manages variable-size

cells in all Cartesian directions. This is most notable in the z-direction, as the program drastically reduces mesh size inside the copper cladding and substrate while increasing cell size in free space regions above and below the structure.

Adaptive meshing increases simulation time, but reduces overall RAM requirements. In the best case, the original 1.5 GHz design with adaptive meshing requires 40 million cells. Additional changes are required to meet the 30 million cell upper limit.

3.6 Gap-Loading

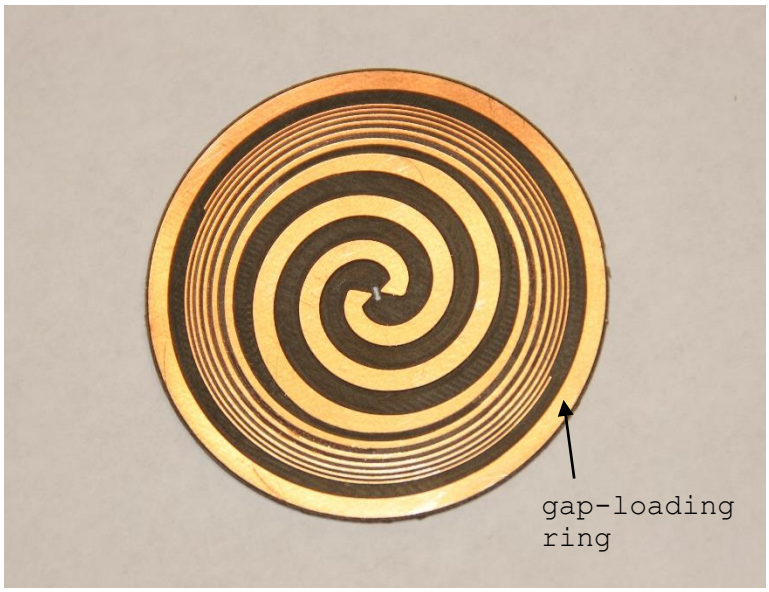

Figure 14: Combination spiral with gap-loading ring. Gap-loading is a space-efficient method of reducing antenna cutoff frequency.

The conductive ring around the spiral shown in Figure 12 and Figure 14 is to achieve gap-loading [15]. Gap-loading utilizes a capacitive frame around the antenna edges to control the initial resonant frequency of the structure. This decreases the effective UWB spiral cutoff frequency, allowing for size reductions of up to 30% [16]. The capacitive frame has a large feature size, adding a minimal number of cells. With this addition, simulations with less than 30 million cells achieve expected performance.

3.7 Power Spiral Order (n) Limitations

Figure 9 shows that increasing order (n) dramatically improves group delay performance. However, values of n greater than 6 cause the outer arms of the spiral to shrink incredibly quickly as the number of turns increases, reducing the feature size to the 0.2mm fabrication limit before the desired cutoff frequency is reached. Trial and error simulations reveal that the n = 6 spiral is the upper limit on power spiral order within the fabrication tolerance constraint of 0.2mm.

4. FABRICATION

All micro-strip spirals are fabricated using an LPKF ProtoMat S100 PC board router tool equipped with a vacuum table [13] to hold the substrate in place during the milling process.

4.1 Manufacturing Errors

The inherent flexibility of the 0.79mm Rogers RT5880 material combined with the applied force and slightly uneven vacuum table surface led to uneven etching. This required custom re-milling of individual sections of each spiral.

The non-planar copper surface combined with the thin substrate also led to issues involving the milling bit depth. Slight milling depth overshoots caused by raised material sections material reduced spiral arm width in some areas. This issue was mitigated by re-etching each section of the spiral while progressively lowering the bit for each run and visually confirming bit depth until all the necessary copper cladding was removed. This iterative method was not perfect, and analysis of results will be necessary to determine milling flaw effects on overall performance. Once the antennas are milled, a microscope and a razor blade are used to cut away any excess copper.

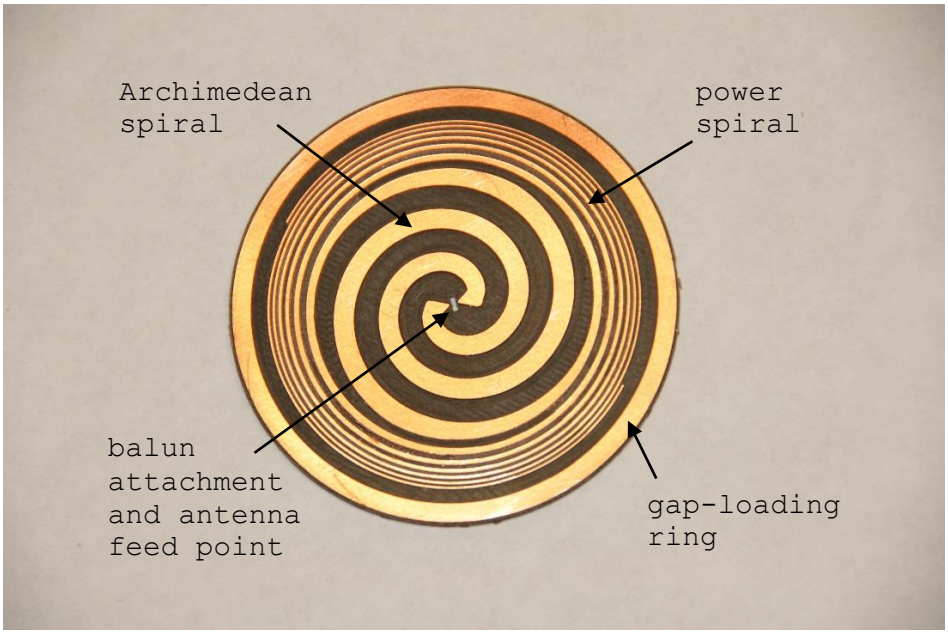

Figure 15: Final design iteration 1.5GHz combination spiral after the milling process. A slot is drilled between the feed points to mechanically accept the tapered balun.

4.2 Balun Transformer

Spiral antennas require differential feeds similarly to dipole antennas. However, the SMA cables used to connect and test the antennas provide single-ended signals, which consist of a signal path and a ground path. In contrast, a differential signal consists of two identical 180° out of phase signals. The conversion from single-ended to differential signals is accomplished by a device called a balun. The basic operation of a balun is illustrated in Figure 16.

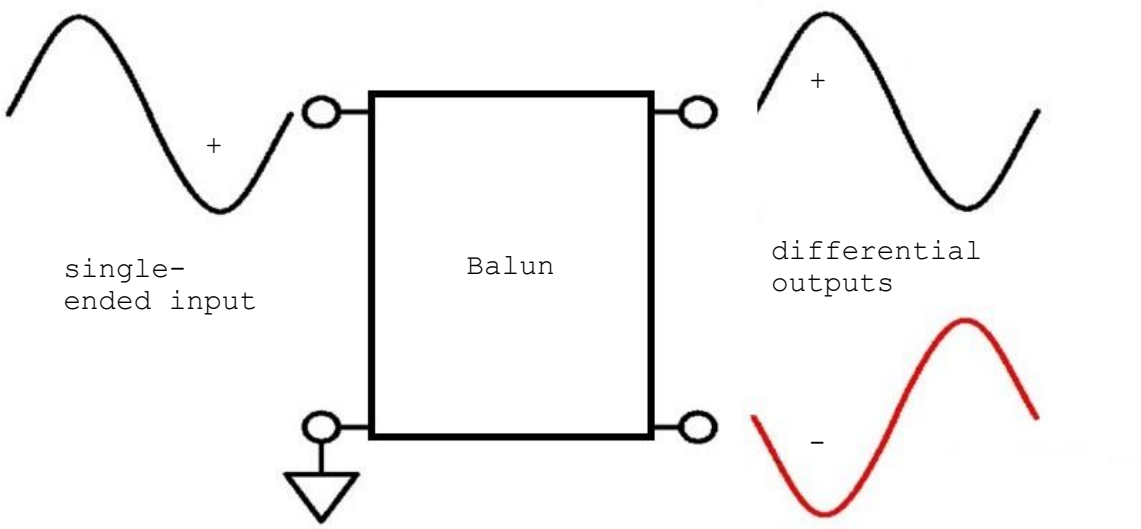

Figure 16: Basic operation of a balun, which converts a single-ended signal (+, GND) into a differential signal (+, –). Similar to dipole antennas, spiral antennas require differential inputs.

Additionally, antenna impedance is not matched to the 50Ω SMA transmission line impedance. An Archimedean spiral in free space has a theoretical input impedance of 188.5Ω [17]. Many balun designs act as impedance transformers, combining the balun and the impedance transformer into a single device. The balun design in Figure 17 is chosen for testing. It utilizes an exponential taper and coupling to produce a differential signal at the antenna input. By providing the input signal to the exponentially tapered side and connecting SMA ground to the linearly tapered side, a differential signal is produced at the antenna end. The baluns are fabricated using the same RT5880 substrate and S100 routing machine.

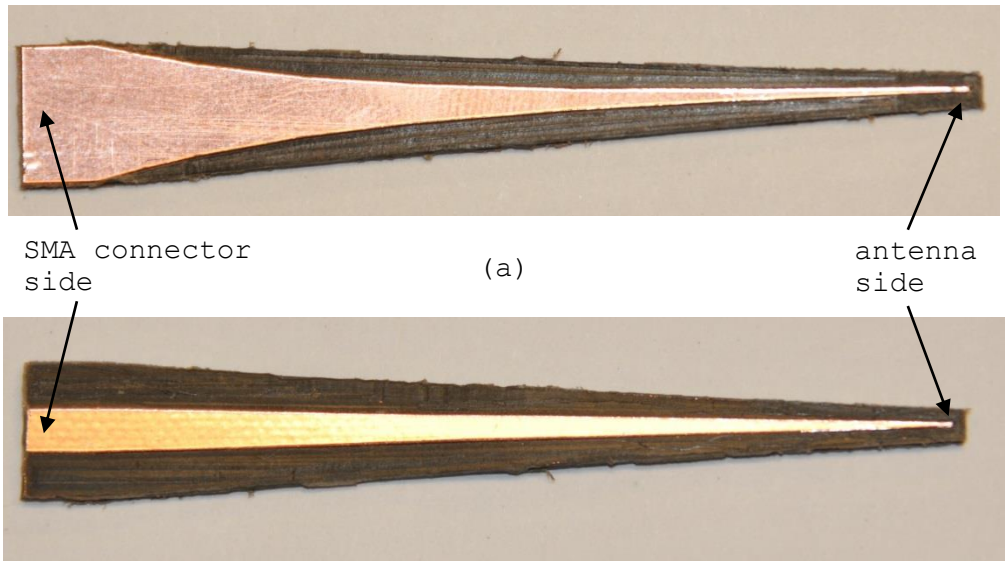

Figure 17: Balun after the milling process. (a) The exponentially tapered side. (b) The linearly tapered side

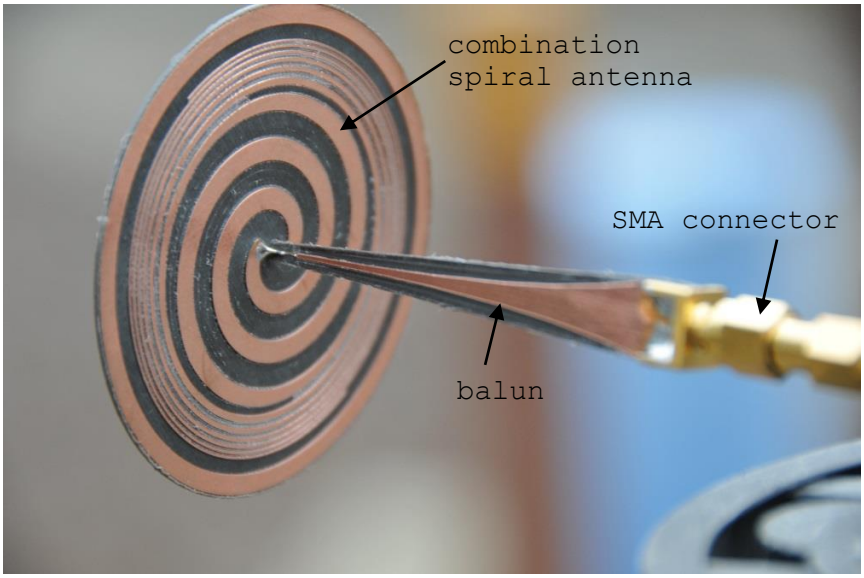

Figure 18: Balun-antenna connection. While this balun is convenient for testing the combined spiral, any balun and impedance transformer can be used depending on system requirements.

5. TESTING

To evaluate the performance of the combination spiral antennas, identical testing processes are performed on the five antennas of interest (see Figure 19): hexagonal horn (H), planar horn (P), Archimedean spiral (A), 3 GHz combination spiral (C3), and 1.5 GHz combination spiral (C1.5). The Archimedean spiral is included in the test to quantify manufacturing errors. Since the Archimedean spiral design has been studied in depth and was manufactured using an identical process to the combination spirals, it should be possible to determine negative milling process effects upon the combination spiral results [18] [19]. The planar horn is an alternative design under development for the same ground-penetrating radar application. Comparing performance at this stage is revealing, however the planar horn is in a much later development stage relative to the combination spiral; any negative comparisons should be considered accordingly.

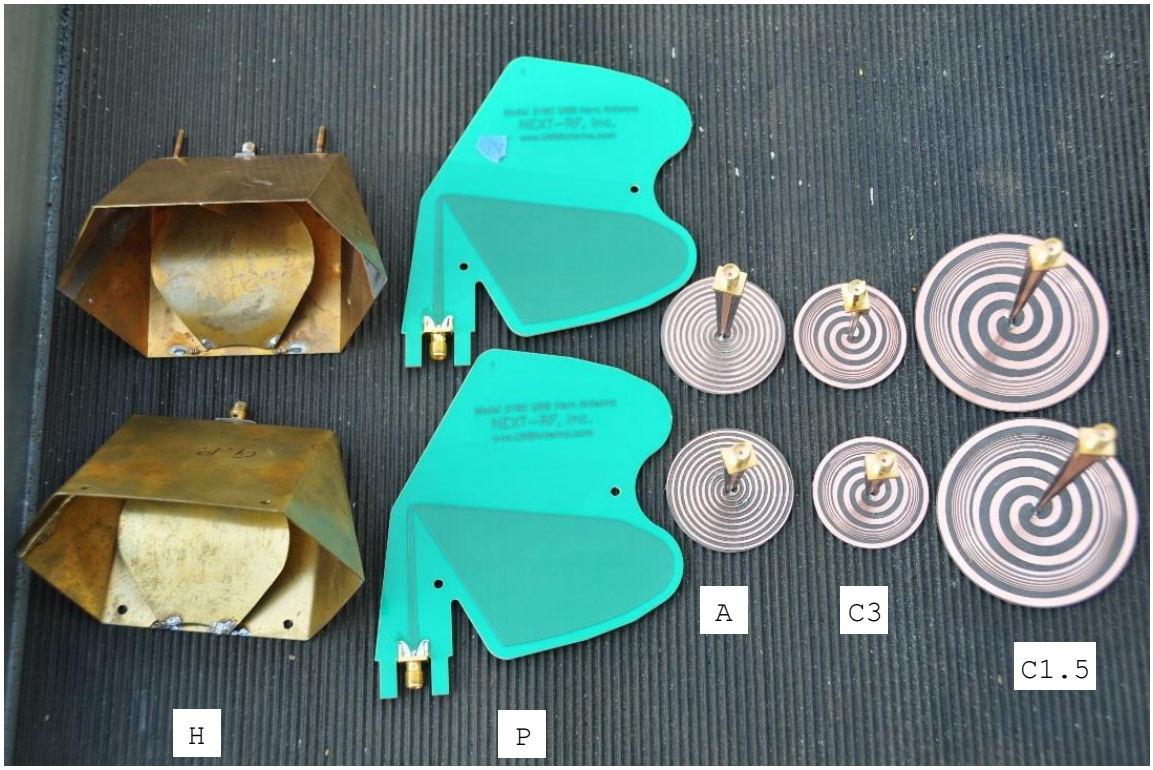

Figure 19: Devices under test (DUTs). From left to right: hexagonal horn (H), planar horn (P), 3 GHz Archimedean spiral (A), 3 GHz combined spiral (C3), 1.5 GHz combined spiral (C1.5). Two of each DUT are necessary for S_{21}, cross correlation, and cross coupling measurements.

5.1 S_{11} (Return Loss)

The S_{11} test setup incorporates a Vector Network Analyzer (VNA) calibrated for a frequency range from 1 GHz to 12 GHz. The S_{11} measurement is based on reflected energy from the transmitting antenna; only Port 1 is active. The DUT is connected to Port 1 via a 5 meter SMA cable. The cable length is removed from the measurement by calibrating the VNA with the cable attached, shifting the reference plane to the DUT input. The DUT is mounted on a wooden tripod and placed as far from physical obstructions

as possible. Both the forward and reverse broadside directions, normal to the substrate plane, are free from obstructions to approximately 25 meters.

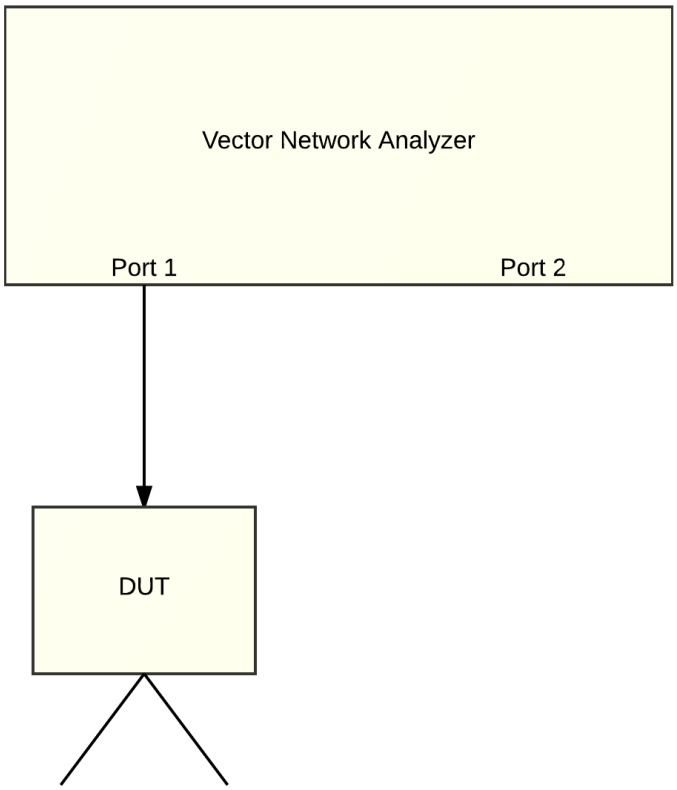

Figure 20: S_{11} measurement connection diagram. Only one of each DUT is needed. This test determines the range of radiated frequencies.

5.2 S_{21} (Gain and Group Delay)

The S_{21} setup incorporates a VNA calibrated for a frequency range from 1 GHz to 12 GHz with both ports active. Each port is connected to an identical DUT through a 5 meter SMA cable.

The antennas are placed to ensure broadside radiation at spacings of 1, 1.5, and 2 meters. These distances are chosen to maintain high power for measurement purposes while remaining in the far-field range, reducing close-range radar clutter that could otherwise effect the results. Equation 10 is used to determine far field distance R, where D is the maximum linear antenna dimension and λ is the minimum wavelength (maximum frequency) of interest.

$$R > {2D^2}/{\lambda} \qquad (10)$$

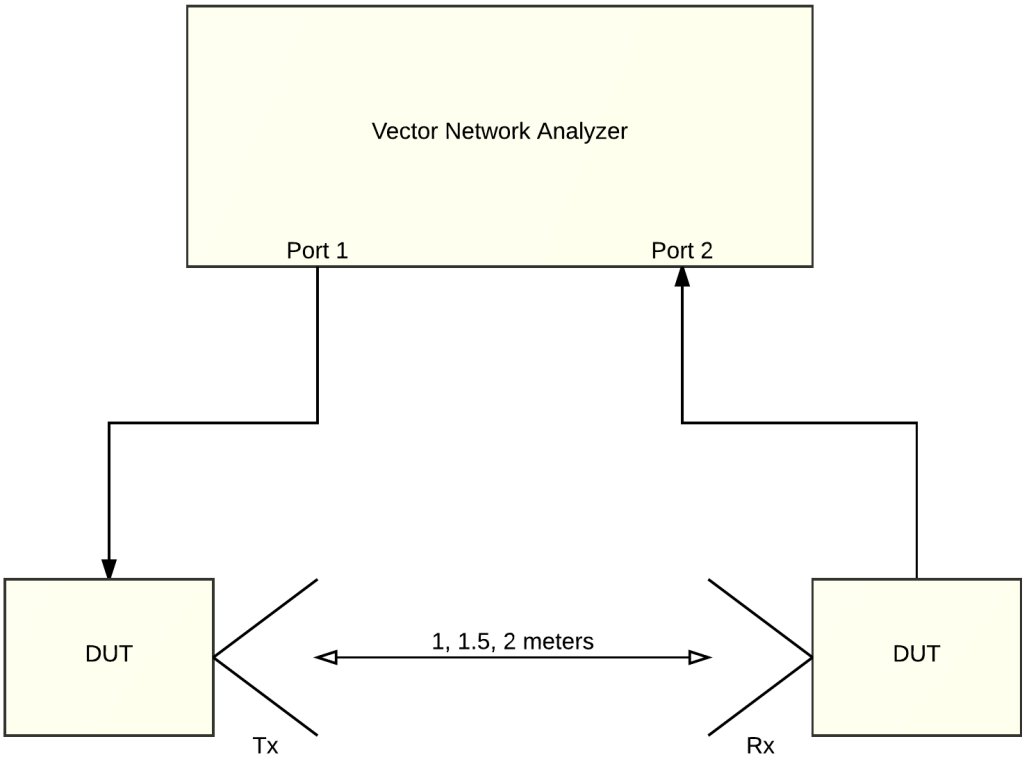

Figure 21: S_{21} measurement connection diagram. DUT spacing is controlled to maintain high gain while remaining in the far field region.

Figure 22: S_{21} measurement test configuration. DUT spacing and orientation is carefully controlled for repeatable measurements. Non-reflective wooden tripods are used to reduce interference.

5.3 Pulse Fidelity

Pulse fidelity information is calculated by transmitting a known pulse through the first DUT and receiving through a second DUT at a spacing that ensures far-field results. The HP 83480A Digital Communications Analyzer is used to capture time-domain information. The results are then evaluated using Equation 5.

Two separate pulse generators are used in this test. The first is a reference Picosecond Pulse Labs Impulse Generator model 3500A set to a 50 kHz repetition rate, 21dB output power and negative

polarity. Both zero and first order pulses are evaluated. This device is used in the measurement scheme shown in Figure 23.

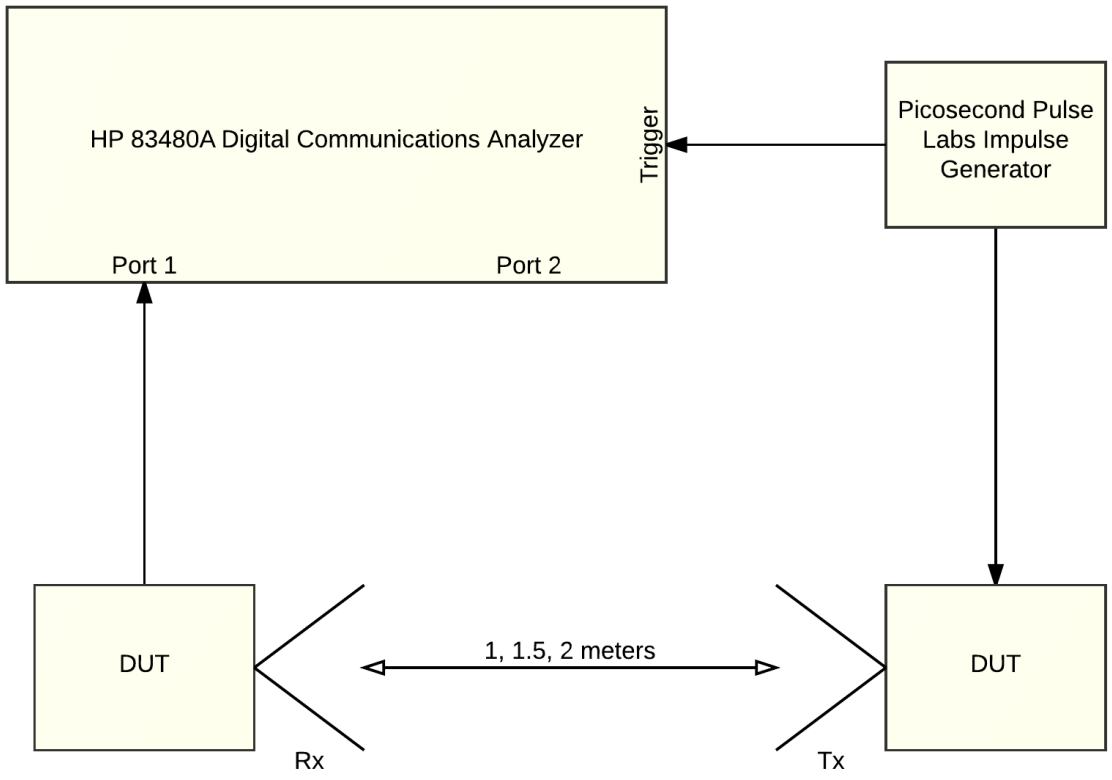

Figure 23: Pulse fidelity measurement connection diagram for the Picosecond Pulse Labs impulse generator. Spacing is controlled to maintain high gain while remaining in the far field region.

The second pulse generator is the JIEDDO 18V Transmitter designed specifically for this ground-penetrating radar system. The JIEDDO 18V Transmitter output power exceeds the HP 83480A input port specifications; hence, a 20 dB SMA inline attenuator is used to prevent damage. Figure 24 shows the test configuration for the JIEDDO pulse measurements. An additional test set includes a 700

MHz diplexer on the pulse generator output with a 50Ω load on the low frequency port, as shown in Figure 25. The diplexer splits the signal into high and low frequency components, eliminating low frequency pulse content that cannot be transmitted by the spiral antennas. The spiral antenna pulse fidelity is expected to improve with addition of the diplexer.

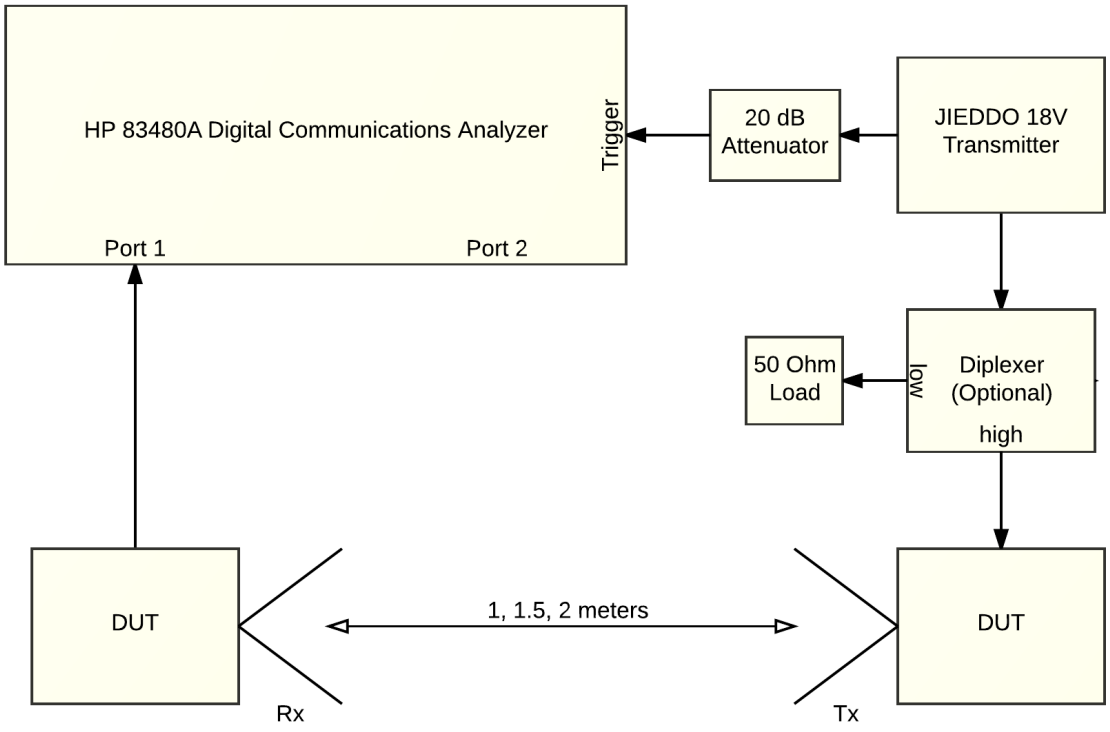

Figure 24: Pulse fidelity measurement connection diagram for the JIEDDO 18V impulse generator. Spacing is controlled to maintain high gain while remaining in the far field region. Additional testing is completed with a diplexer on the pulse generator output.

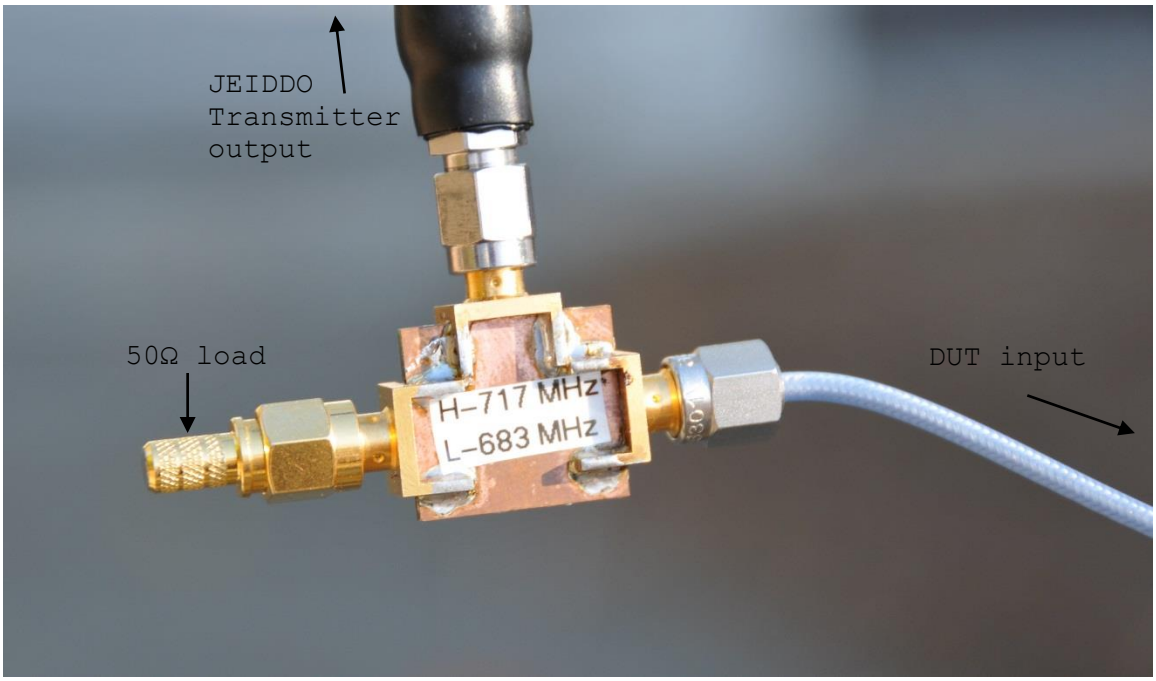

Figure 25: This 700 MHz diplexer with 34 MHz bandwidth splits the input pulse into low and high frequency components. A 50Ω load eliminates the low frequency content which is less than the spiral antenna's cutoff frequency.

5.4 Cross Coupling

The cross coupling measurement is important radar array operation. A linear device array is used to increase the amount of information received from the radar returns, as seen in Figure 5. Each antenna acts as an individual transmitter while the remaining antennas act as receivers. Any information will be received as energy reflecting from target surfaces. However, substantial side-lobes 90 degrees from broadband could cause high power undesired signals to radiate directly between antennas.

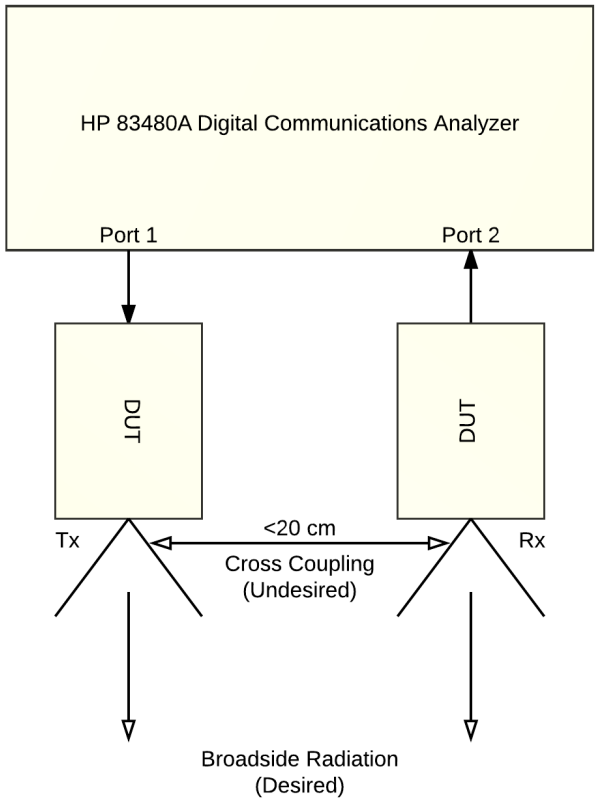

Figure 26: Cross coupling measurement connection diagram. Spacing is maintained as close as possible to maximize received energy for testing purposes.

The cross coupling measurement is performed with a VNA calibrated for the frequency range from 1 GHz to 12 GHz with both ports active. Port 1 is connected to a transmitting DUT via a 5 meter SMA cable, while port 2 is connected to a receiving DUT via a 5 meter SMA cable. The devices are placed facing the same direction; the receiving antenna is 90 degrees broadside to the transmitting antenna and vice versa. The devices are placed as close together as the tripods will allow, approximately 15cm, in order to increase the apparent coupling gain. This spacing is maintained throughout testing.

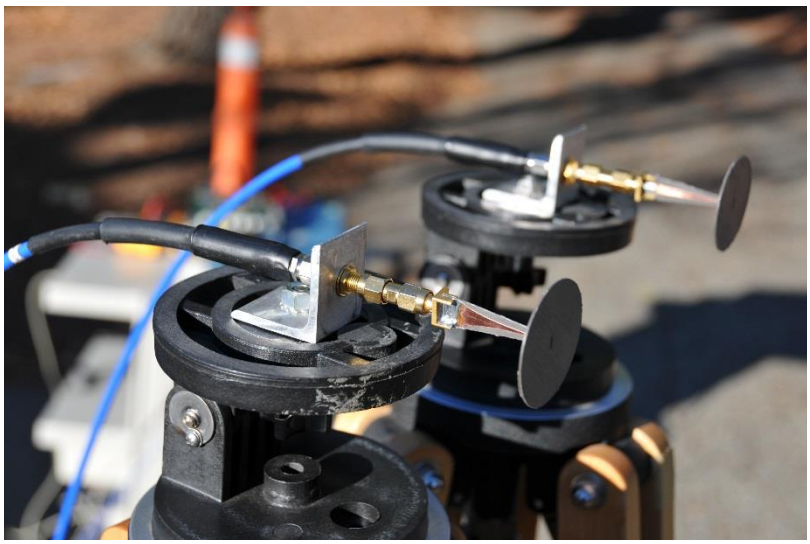

Figure 27: Cross coupling measurement test configuration. Spacing is the minimum capable while mounted on the tripods.

6.1 Return Loss

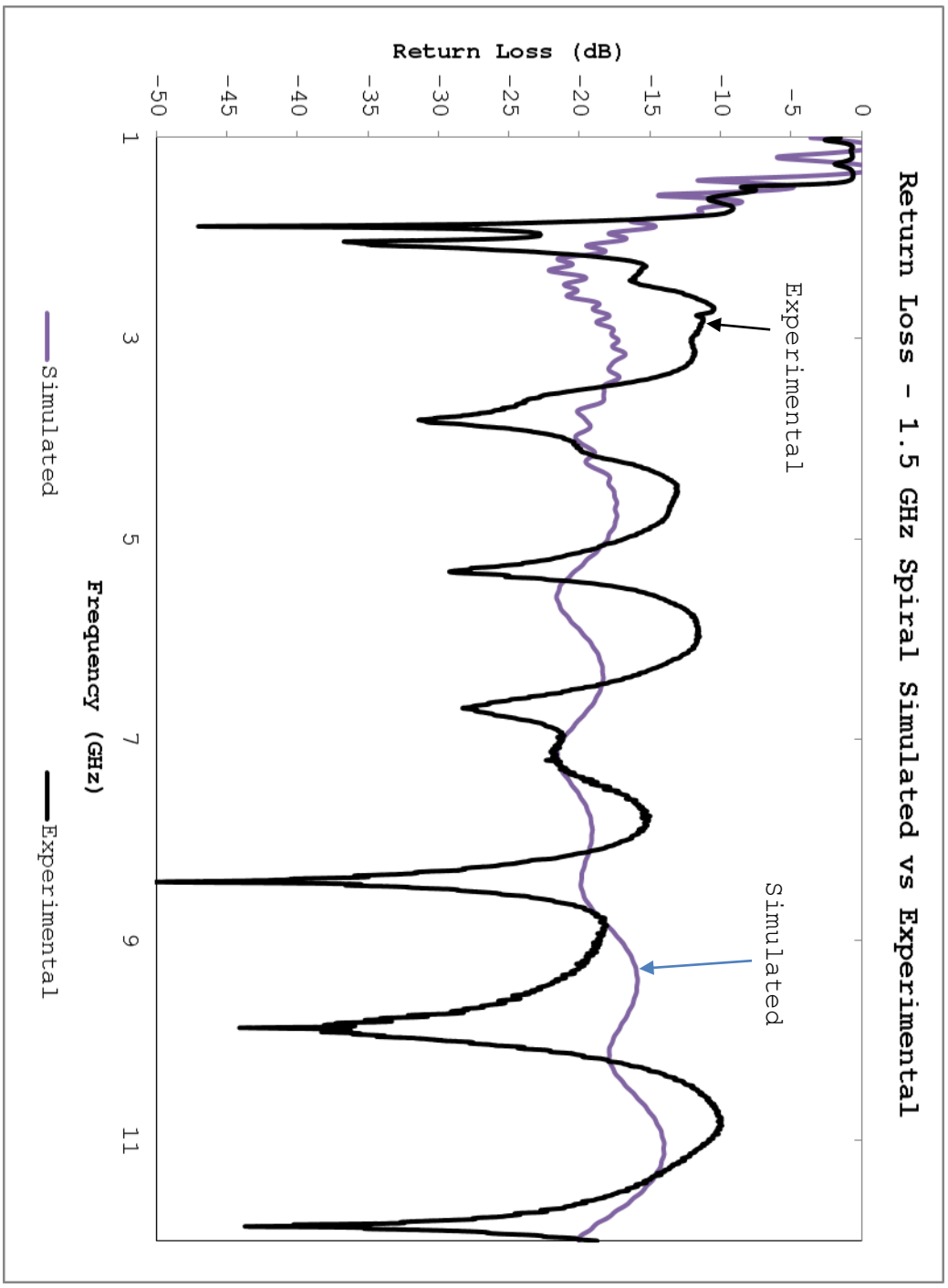

Figure 28: Comparison between simulated and experimental return loss of the 1.5 GHz spiral antenna. Experimental results match expected trends but show undesired periodic frequency response.

Figure 28 compares the 1.5 GHz return loss performance from test results with the expected results from CST simulations. The experimental results achieve the specified passband return loss of -10 dB for all frequencies above 1.5GHz. However, simulated performance is up to 7.5dB better than experimental performance. Additionally, the DUT return loss periodically drops well below the expected range. Comparing the 1.5GHz combined spiral results to the other DUTs, it can be determined whether or not this behavior is design-inherent or an undesired effect of fabrication and testing methods.

Figure 29 and Figure 30 compare S_{11} performance of the 1.5 GHz combined spiral against the horn and spiral antennas, respectively. The planar horn and Archimedean spiral appear to have the lowest return loss in the passband, while the hexagonal horn achieves the greatest matching performance of all the DUTs. The 3 GHz combination spiral design, with parameters matching those of the antenna in the paper that proposed the design, shows a 2.4 GHz cutoff frequency rather than the expected 3.1 GHz. The Archimedean spiral shows similar behavior, with a 2.1 GHz cutoff frequency. Otherwise, return loss performance of all DUTs confirms desired UWB operating frequencies up to 12 GHz.

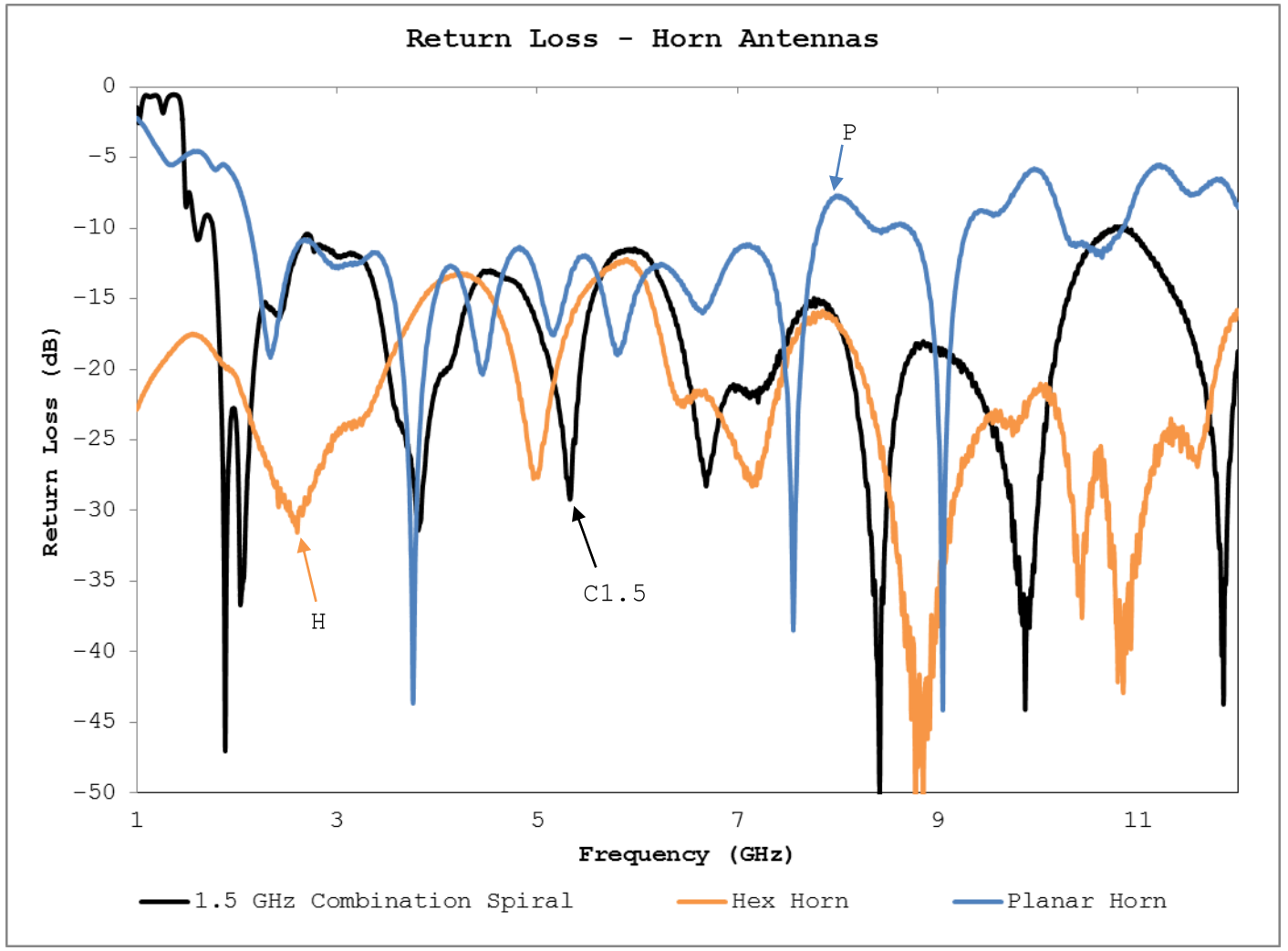

Figure 29: Comparison of return loss performance between the 1.5 GHz combined spiral and the horn antennas. Periodic behavior is consistent across all DUTs, substantiating assumption that test methodology is at fault.

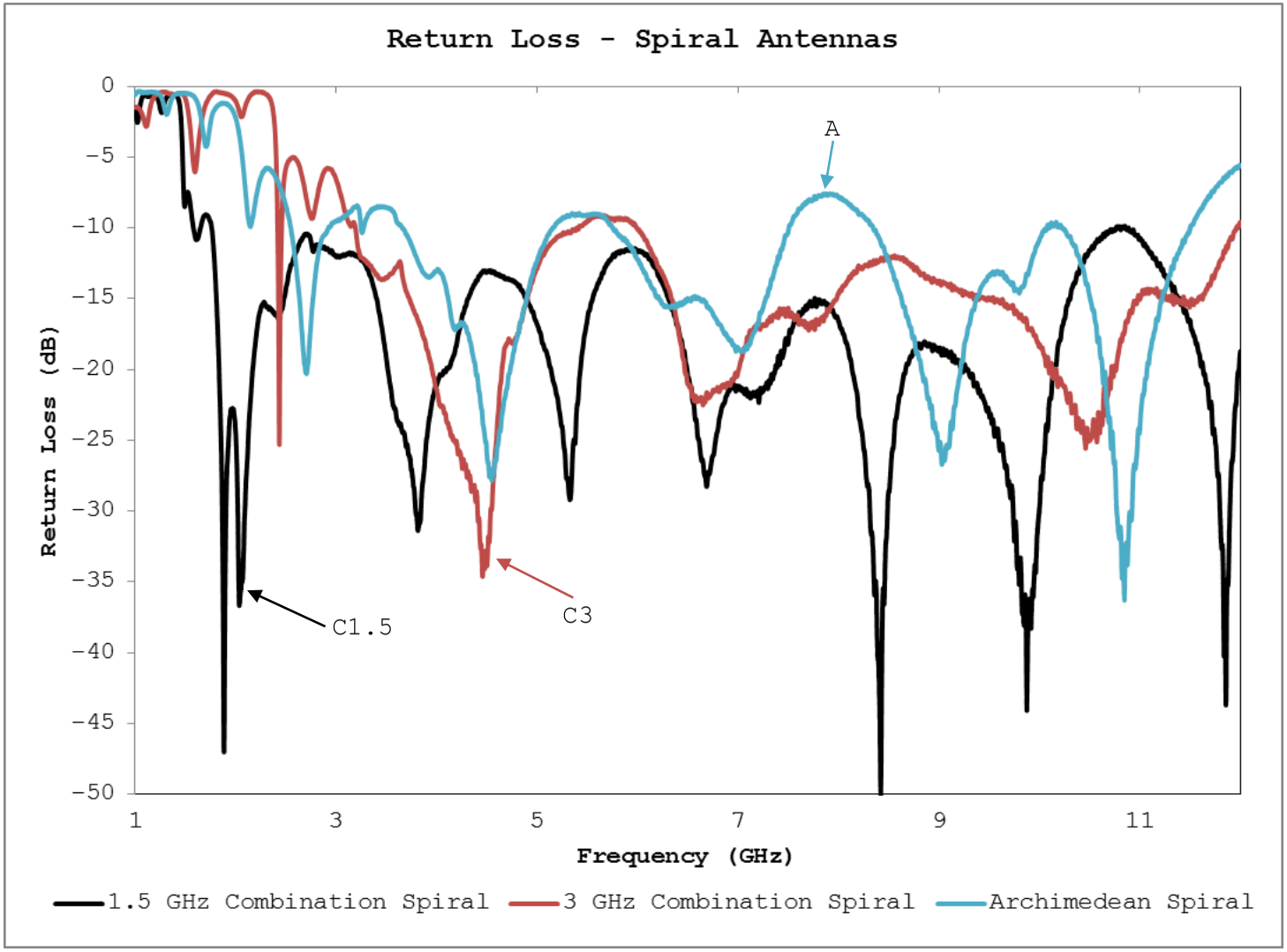

Figure 30: Comparison of return loss performance between the 1.5 GHz combined spiral and the other spiral antennas. Cutoff frequencies of 3 GHz combined spiral and Archimedean spiral lower than expected.

The periodic return loss response is consistent across all DUTs, indicating that the testing methodology is at fault. The two horn antenna designs were not fabricated on the LPKF S100 but still show the same behavior, eliminating the possibility that the fabrication process is the issue. The tests were performed outdoors, with sufficient distance between the antennas and nearby objects to prevent clutter. However, additional testing in an anechoic chamber would eliminate interference from nearby physical objects, providing insight into the cause of the periodicity.

6.2 Gain

Figure 31 and Figure 32 compare gain performance of the 1.5 GHz combined spiral against the horn and spiral antennas, respectively. The horn antennas achieve the highest, averaging approximately 7.5 dB. The Archimedean and 3GHz spirals underperform the 1.5GHz spiral, which achieves the specified 5 dB gain.

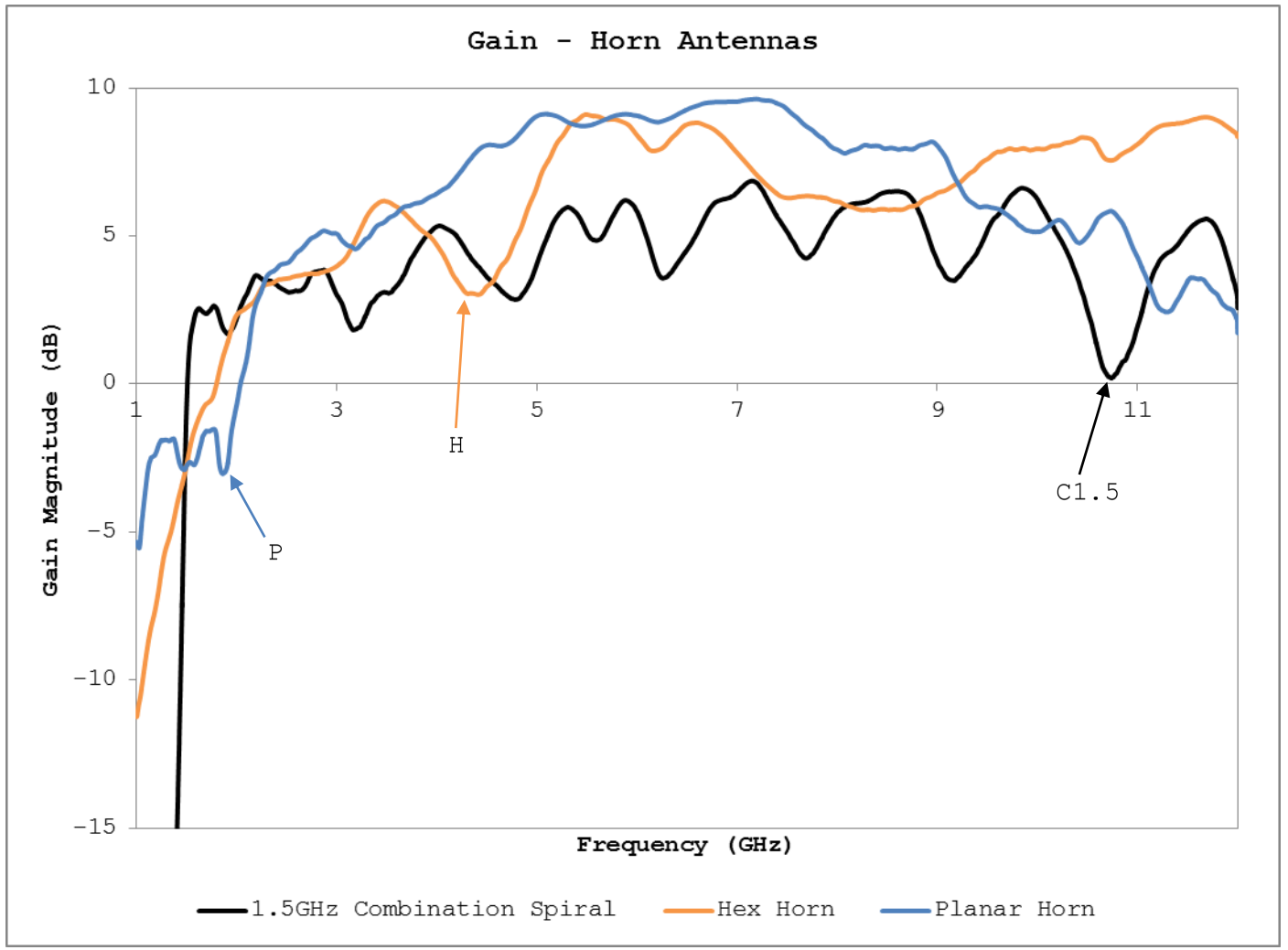

Figure 31: Comparison of gain performance between the 1.5 GHz combined spiral and the horn antennas. The hexagonal horn antenna achieves the highest gain.

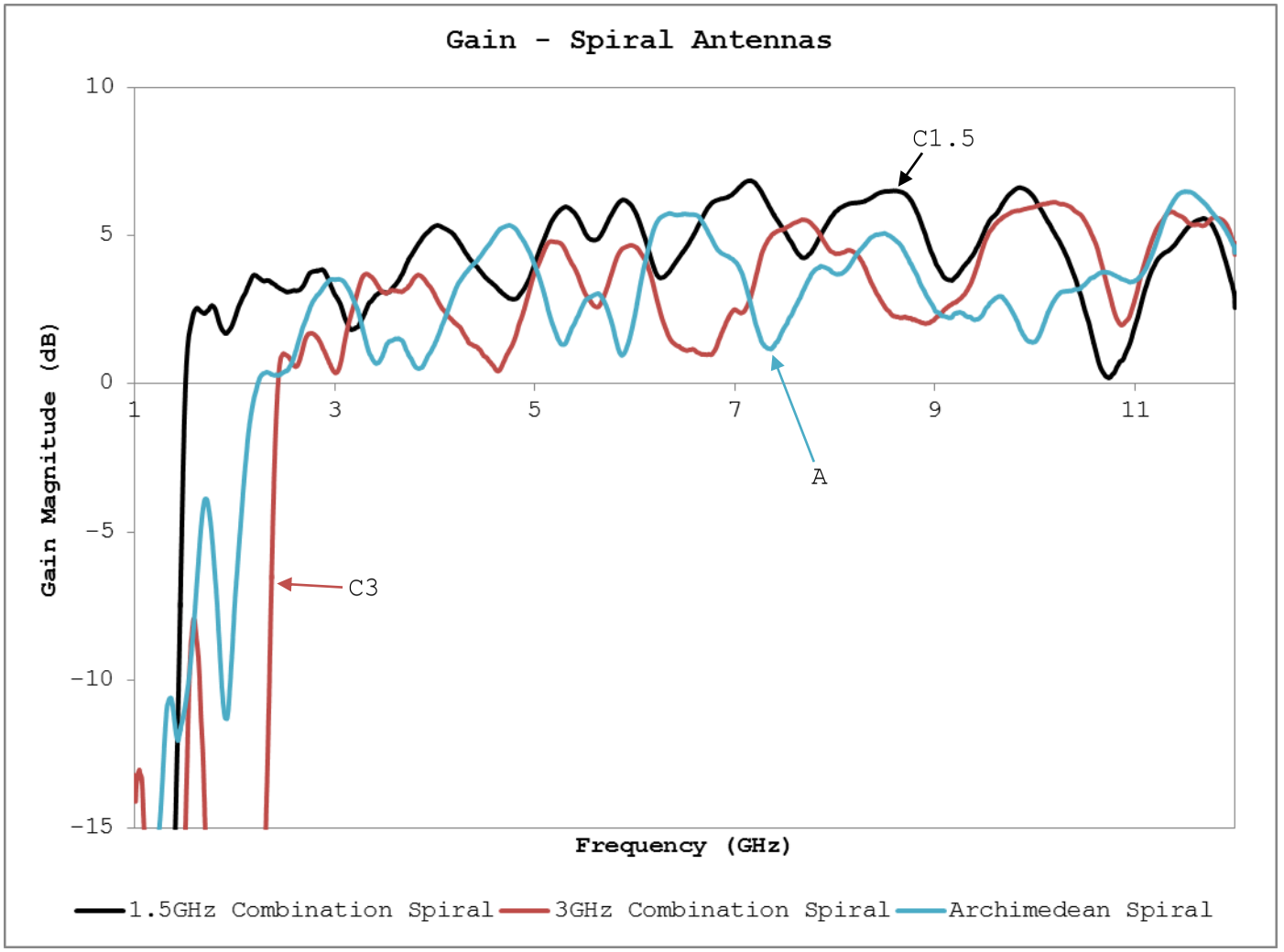

Figure 32: Comparison of gain performance between the 1.5 GHz combined spiral and the other spiral antennas. The 1.5 GHz spiral reaches the 5dB gain specification.

6.3 Group Delay

Figure 33 and Figure 34 compare the group delay performance of the 1.5 GHz combination and Archimedean spirals against theoretical responses from Equation 8. Although the high noise content group delay frequency response hinders results interpretations, measurements appear to match theory.

The 1.5 GHz combination spiral's maximum group delay deviation occurs between 2 GHz and 3 GHz. In this operating zone, the spiral arms are smallest and inaccurate milling processes effects are greatest. It is possible that improving fabrication accuracy could cause results to more closely align with the theoretical solution.

Figure 35 and Figure 36 compare the group delay performance of the 1.5 GHz combined spiral against the horn and spiral antennas, respectively. Due to the low horn antenna operating frequency, group delay remains relatively constant down to 1 GHz as expected. Figure 9 shows that spiral antenna group delay spikes as frequencies approach cutoff. Comparing the 3GHz combined spiral against the 3 GHz Archimedean spiral, Figure 36 confirms that the combined spiral achieves constant group delay over a wider frequency range than the Archimedean spiral.

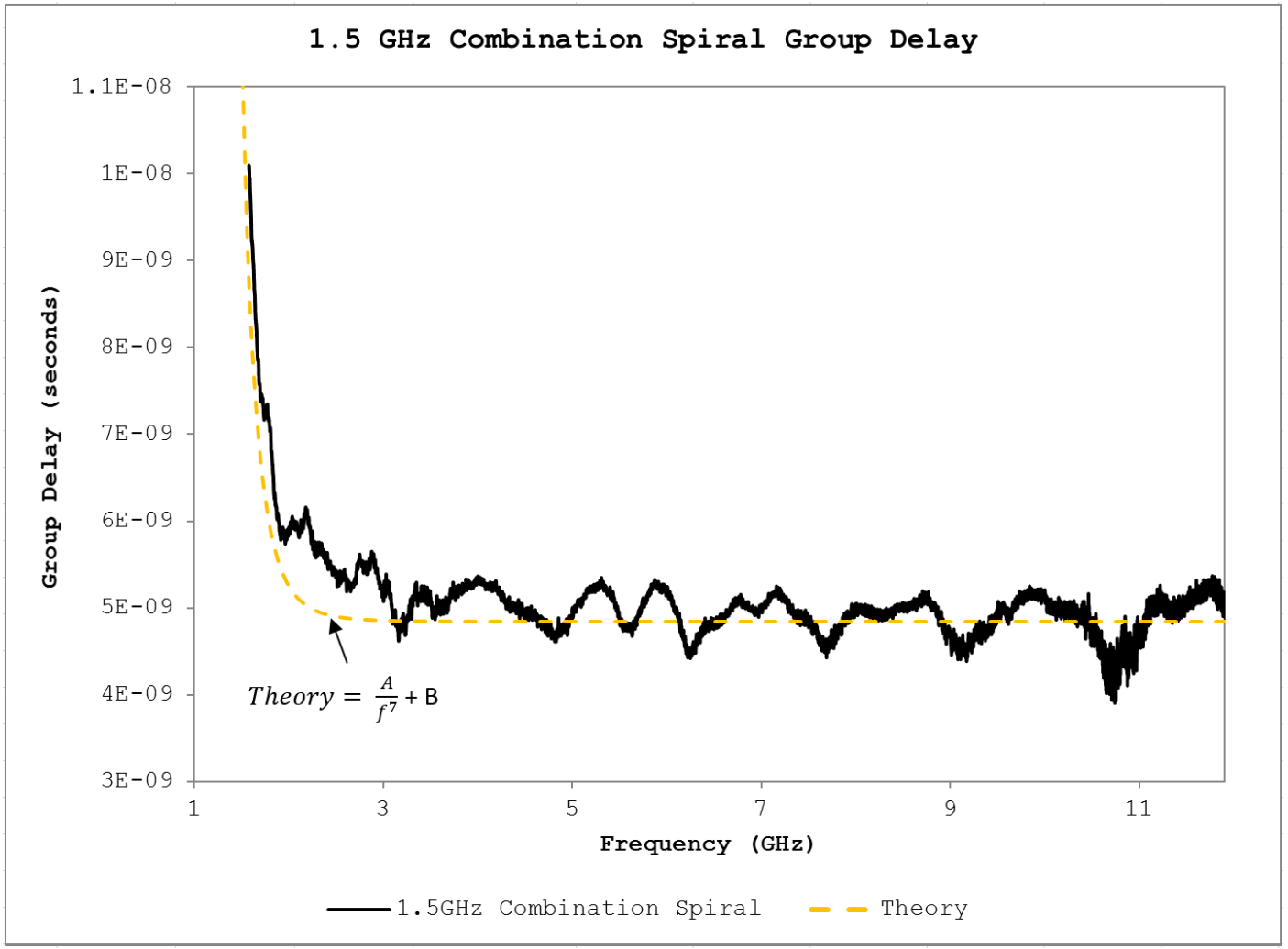

Figure 33: Comparison of 1.5 GHz combination spiral group delay results with theoretical calculations.

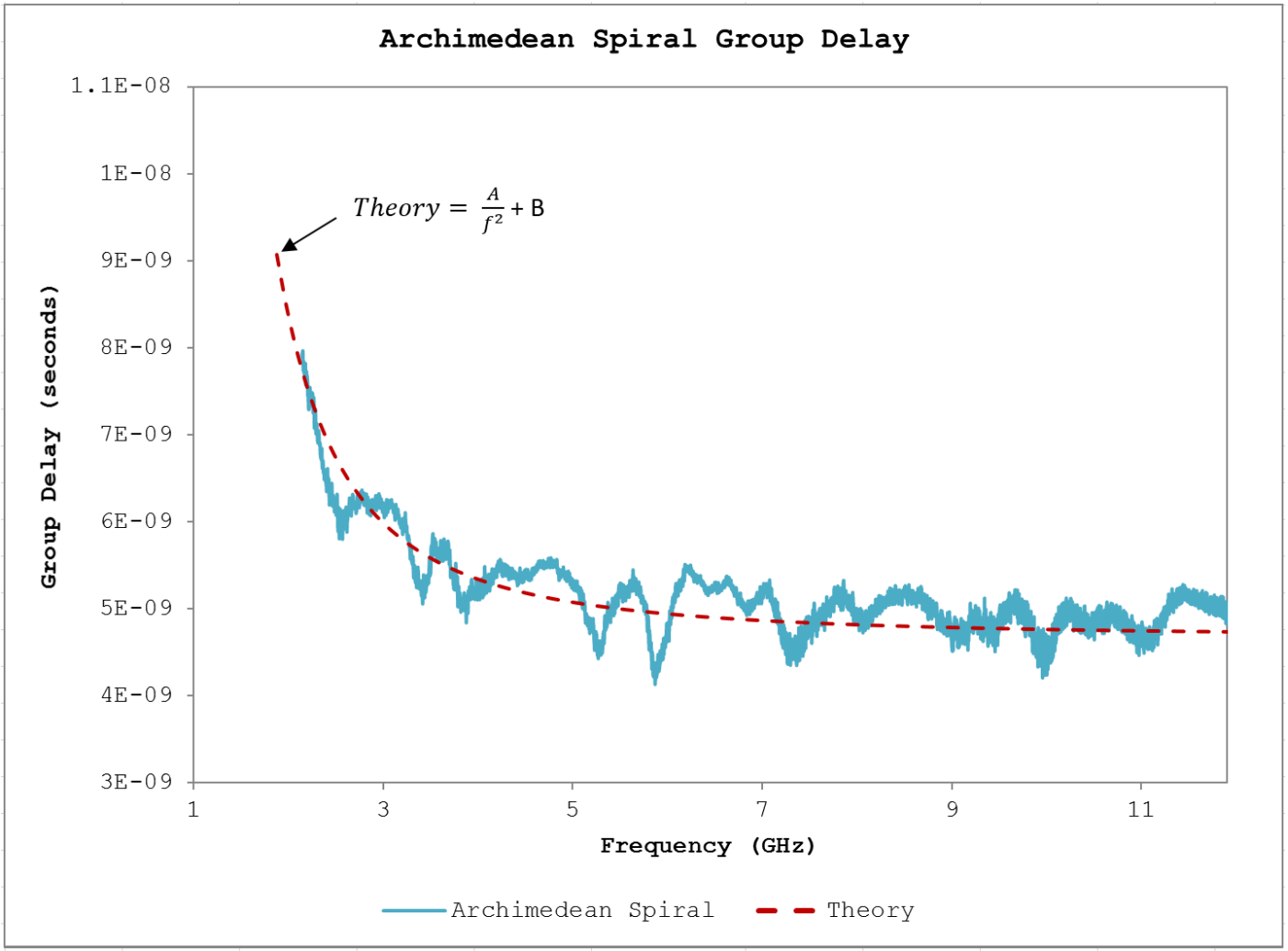

Figure 34: Comparison of Archimedean spiral group delay results with theoretical calculations

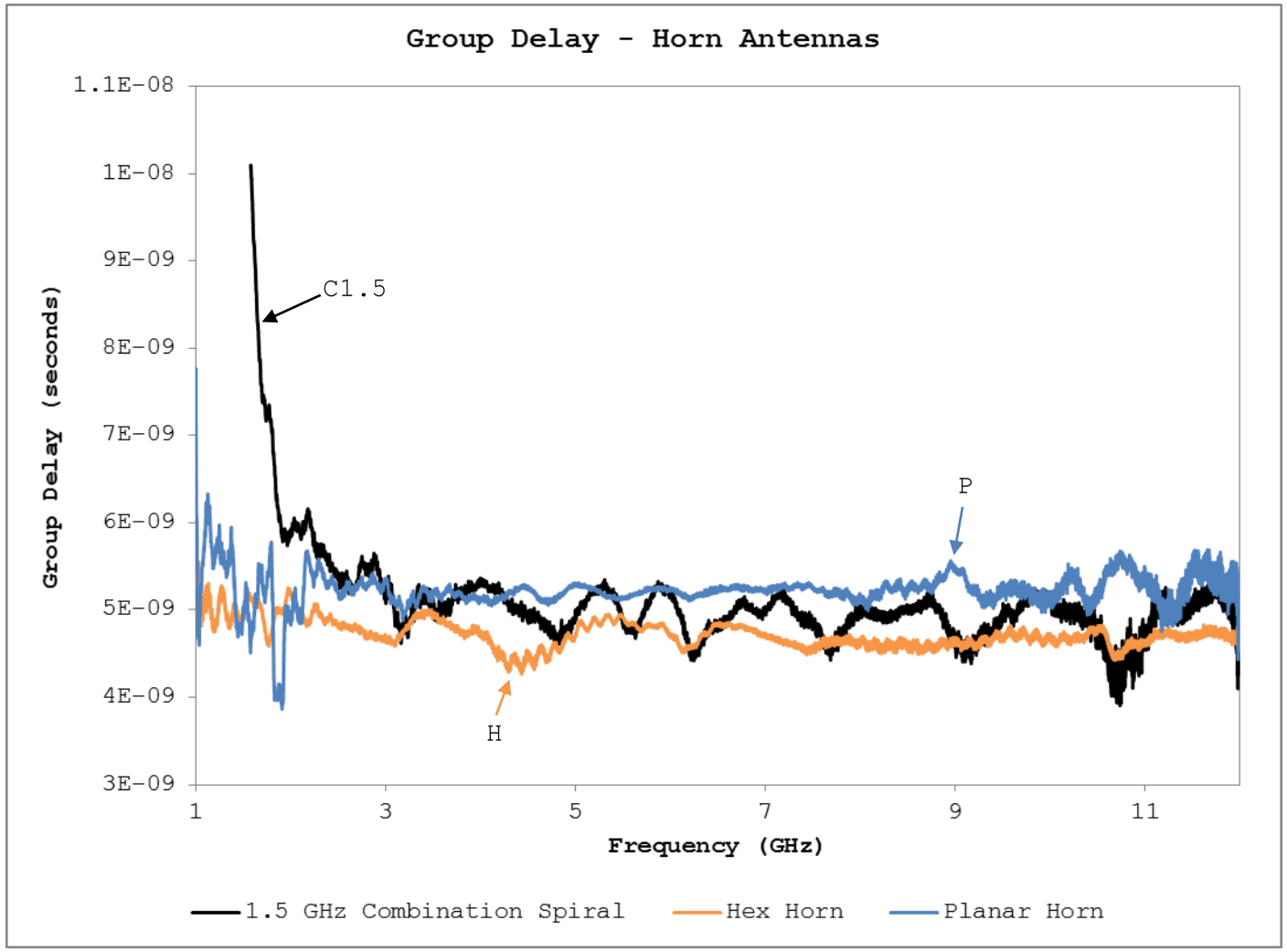

Figure 35: Comparison of group delay performance between the 1.5 GHz combined spiral and the horn antennas. Results confirm the excellent horn antenna performance at low frequencies.

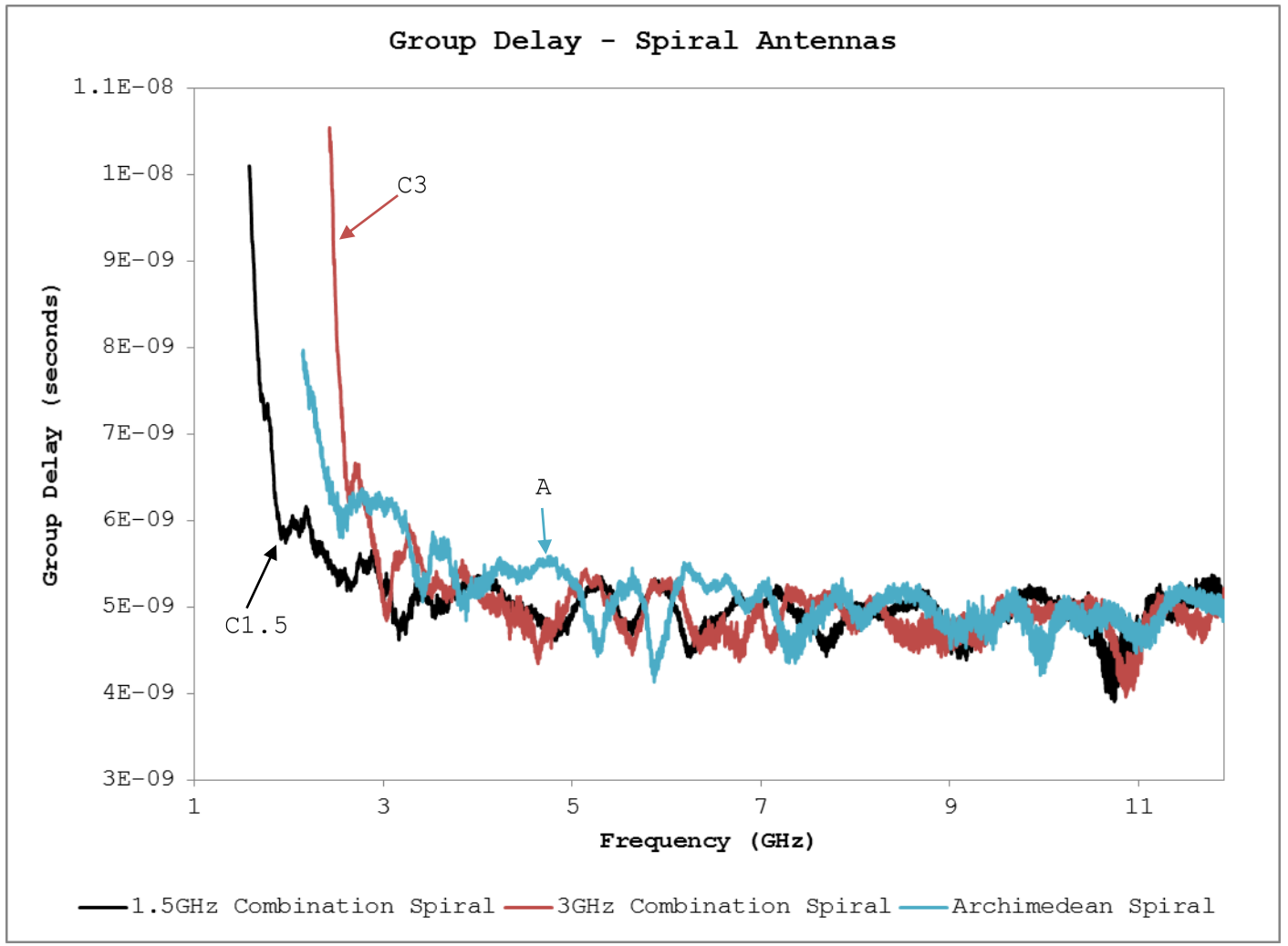

Figure 36: Comparison of group delay performance between the 1.5 GHz combined spiral and the other spiral antennas. Experimental results appear to match theory.

Due to the erratic behavior of the group delay response, no further information can be gathered from these figures directly. Maximum cross correlation calculations will be used to clarify performance differences between the DUTs.

6.4 Pulse Fidelity

Table 3 summarizes pulse fidelity results from all four test cases. Time domain results are shown in Figure 39 through Figure 50 in Appendix A. For the purpose of comparison, absolute pulse fidelity values are less important than relative performance. Comparing the 1.5 GHz spiral against the 3 GHz design reveals that lower cutoff frequencies cause pulse fidelity improvement in every test. This agrees with expected performance, given that the lower frequency spirals are capable of radiating a larger range of frequency content. It also agrees with simulation results shown on the bottom of

(b)

Table 3. This trend can likely be extrapolated to lower frequency designs. It is possible that with a sufficiently low cutoff, pulse fidelity of the combined spiral could rival that of the horn antennas. However, additional testing is necessary to confirm this assumption.

	Archimedean Spiral	**3 GHz Combination Spiral**	**1.5 GHz Combination Spiral**	**Hex Horn**	**Planar Horn**
Pulse Converter - 0 order	0.2346	0.2583	**0.266**	0.3905	0.3185
Pulse Converter - 1st order	0.3477	0.3856	**0.4764**	0.4757	0.6237
18V Impulse Transmitter	0.0749	0.0529	**0.1075**	0.1543	0.2307
18V Impulse Transmitter w/ Diplexor	0.1526	0.1536	**0.18**	0.502	0.5071
Simulation		0.837	**0.942**		

(a)

$$F = \max_{\tau} \left| \frac{\int_{-\infty}^{\infty} a(t) r(t+\tau) dt}{\sqrt{\left(\int_{-\infty}^{\infty} a(t)^2 dt\right)\left(\int_{-\infty}^{\infty} r(t)^2 dt\right)}} \right|, \; 0 \leq F \leq 1$$

(b)

Table 3: (a) Pulse fidelity summary. Results indicate that decreasing combined spiral cutoff improves cross correlation, as expected from simulation results. (b) Pulse fidelity formula from Equation 7. Pulse fidelity values are between 0 and 1, indicating performance from perfectly uncorrelated to perfectly correlated, respectively

The Archimedean and 3 GHz combined spirals were designed with identical operating frequencies, enabling direct comparisons. However, as shown in Figure 30, the resulting cutoff frequencies were much lower than expected, 2.1 GHz for the Archimedean spiral and 2.4 GHz for the combined spiral. While the combined spiral shows improvement in most cases, the 18V JIEDDO transmitter without a diplexer achieved improved pulse fidelity performance through the Archimedean spiral. This is likely due to the lower cutoff frequency of the Archimedean spiral. The fact that the combined spiral achieves a better pulse fidelity in many tests despite having a higher cutoff confirms the benefits of the combined spiral design.

6.5 Cross Coupling

Figure 37 and Figure 38 compare time domain results of the 1.5 GHz combined spiral to the other DUTs oriented 90 degrees off broadside. Absolute values of these results are not as important as the comparisons between devices. All three spirals perform similarly, revealing small but non-zero returns. The hexagonal horn’s waveguide causes nearly zero received energy. Planar spiral performance is significantly worse, revealing voltage returns of up to 8 times those of the spirals.

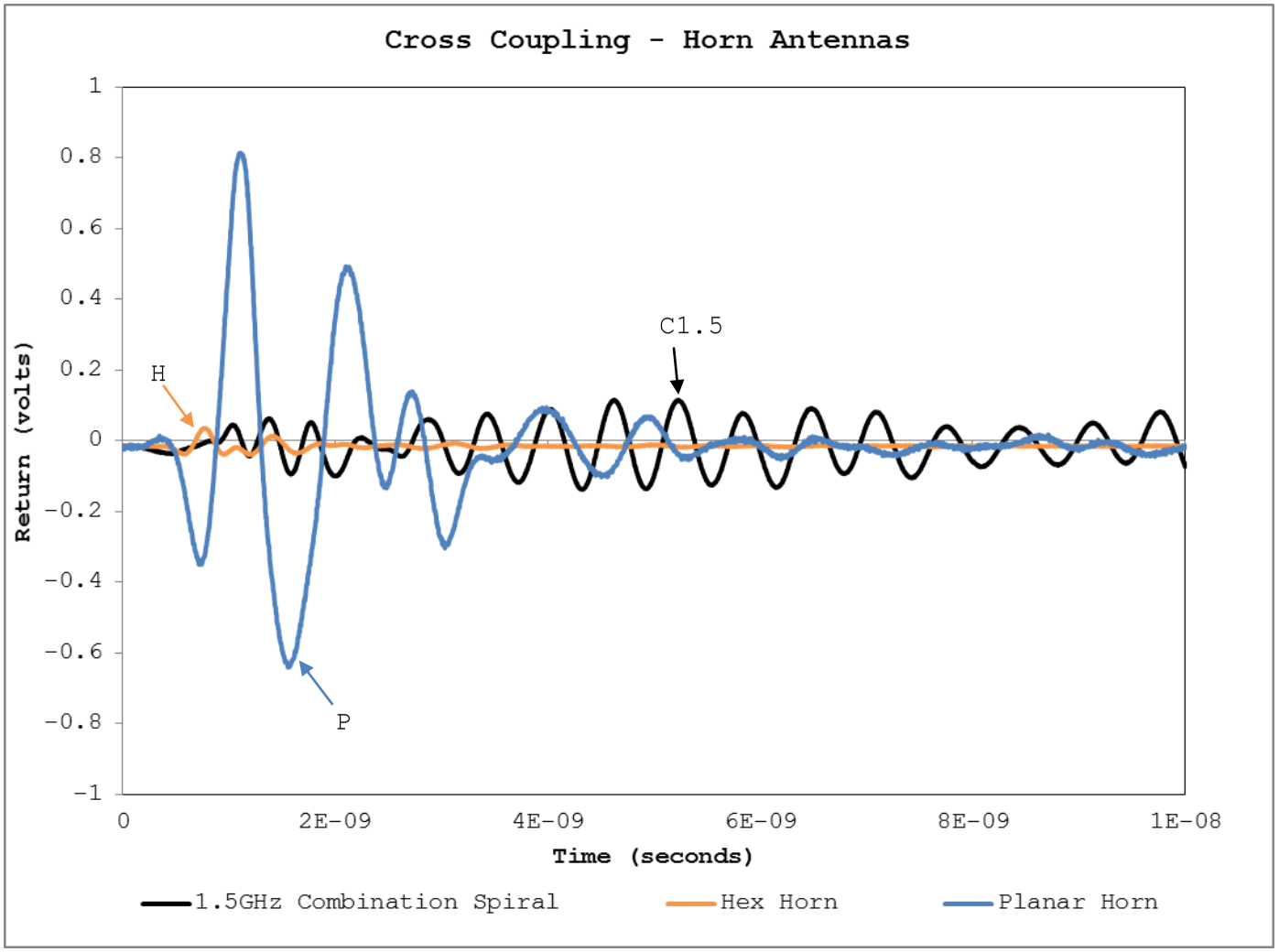

Figure 37: Comparison of cross coupling performance between the 1.5 GHz combined spiral and the horn antennas. Planar horn coupling is highest while hexagonal horn coupling is near zero, as expected.

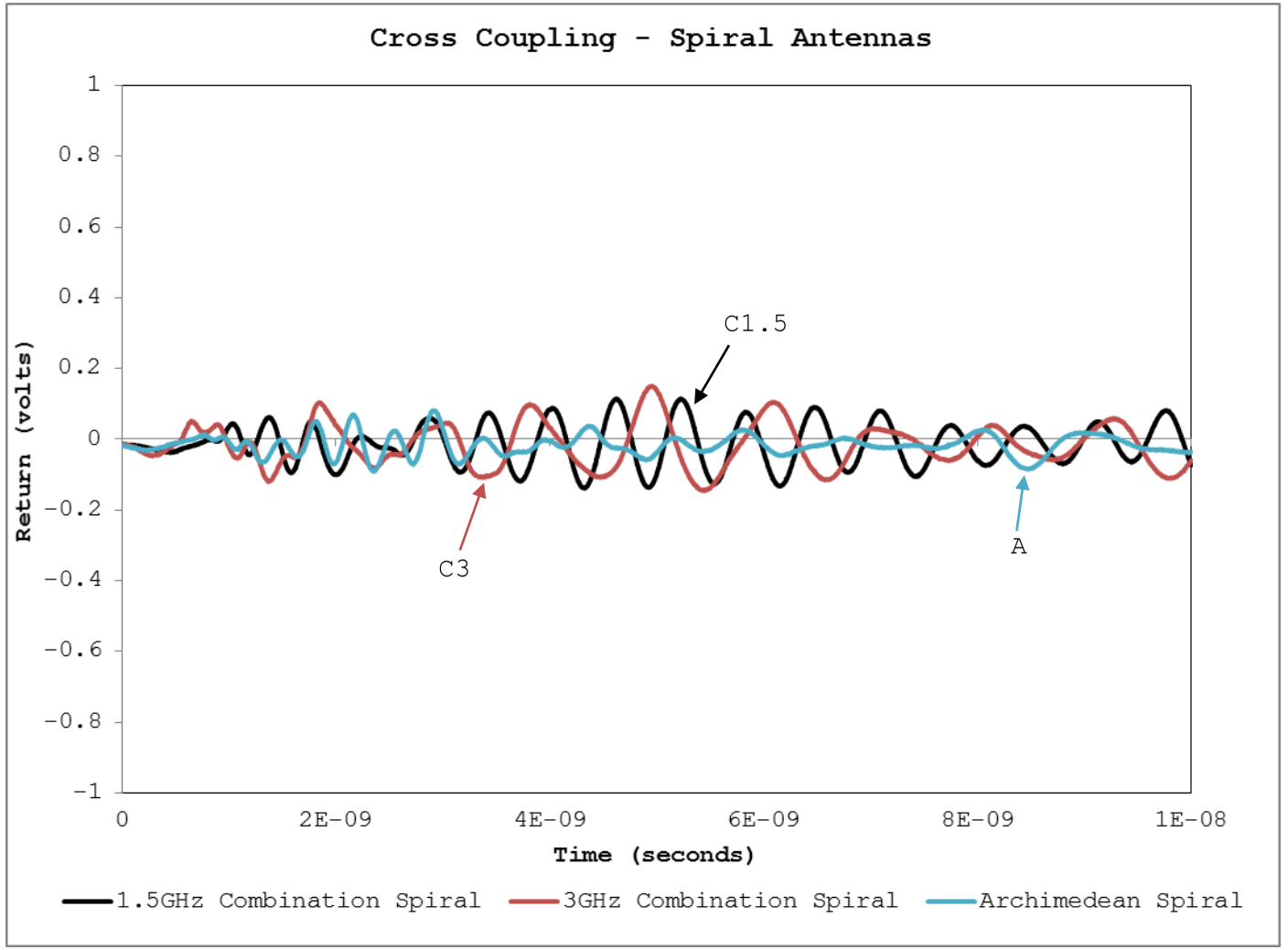

Figure 38: Comparison of cross coupling performance between the 1.5 GHz combined spiral and the other spiral antennas. Performance is consistent across all spiral DUTs as expected.

	Specification	1.5 GHz Combination Spiral (C1.5)	Hex Horn (H)
Cutoff Frequency	800 MHz	1.5 GHz	~ 0 GHz
Passband Return Loss	< -10 dB	-10 dB	~ -15 dB
Pulse Fidelity	> 0.5	0.47 (best)	0.502 (best)
Change in Group Delay above Cutoff	< 0.5 ns	~ 3 ns	~ 2 ns
Gain	5 dB	~ 5 dB	~ 7 dB

Table 4: 1.5 GHZ combined spiral and hex horn results comparison to specifications. The cross correlation values listed are the best case examples; general performance is shown in(a)

(b)

Table 3. Horn antenna performance is higher in every category, however the combination spiral pulse fidelity is competitive.

Table 4 summarizes testing results for the competing low-frequency antennas, the 1.5 GHz combination spiral and hexagonal horn antennas. The hex horn design shows improvement over the combination spiral in every measured parameter. However, the close pulse fidelity results reveal that, with the appropriate

pulse generator, the 1.5 GHz combination spiral performance can rival the hex horn.

It was not possible to create a combination spiral that achieved the specified 800 MHz cutoff frequency with available hardware. However, significant pulse fidelity improvement is shown in Table 3 between the 3 GHz and 1.5 GHz combination spirals due to decreasing cutoff frequency. This indicates that further cutoff frequency reduction by using either a larger or denser spiral will continue to improve pulse fidelity. Additional testing and a higher resolution fabrication process are required to characterize this improvement.

	Archimedean Spiral (A)	3 GHz Combination Spiral (C3)
Cutoff Frequency	2.1 GHz	2.4 GHz
Passband Return Loss	-8 dB	-10 dB
Pulse Fidelity	0.3477 (best)	0.3856 (best)
Change in Group Delay above Cutoff	2.0 ns	1.6 ns
Gain	3.0 dB	3.0 dB

Table 5: Comparison between the 3 GHz spiral designs; the Archimedean and combination spirals. The improvement in pulse fidelity and group delay that the combination spiral demonstrates compared to the Archimedean spiral is confirmation that the combination spiral design possesses inherently lower dispersion.

Table 5 compares the 3 GHz combination spiral antenna against the 3 GHz Archimedean spiral antenna to confirm the conclusions of the Low-Dispersion Spiral Antennas article [7]. The combination spiral shows improved pulse fidelity compared to the Archimedean spiral despite having a higher cutoff frequency. As seen in Figure 19, these two antennas are similar in size. Therefore, the combination spiral's superior pulse fidelity and group delay appears to be solely due to its inherently lower-dispersion design.

8. FUTURE WORK

8.1 Conical Spiral

One disadvantage to planar spiral designs is their low gain. Spiral antennas radiate broadside to the spiral plane in both forward and reverse directions. For ground-penetrating radar applications, this causes two issues; half of the radiated energy is fired away from the target of interest, reducing return power by 3dB, and excess radiated energy reflects causing interference with receive antennas. Interference could be resolved using a microwave absorbing backplane, however this increases design cost and complexity.

A solution to this problem is the conical spiral [11]. Conical spirals, while based upon planar spiral design equations, have an upward extruded center, maintaining the broadside 2D spiral pattern but creating 3D arms that spiral upward as if on the surface of a cone. The void in the cone's center causes destructive interference, eliminating any energy emanating away from the target, increasing antenna gain.

8.2 High Resolution Milling Process

One of the drawbacks of the spiral antenna compared to the existing horn antenna designs is the low frequency radiation. UWB horn antennas operate from high frequencies all the way down to DC, increasing the radiated frequency content and improving radar system performance. Low frequency signals cannot be radiated in a spiral antenna due to the finite length of the spiral arms. However, due to the nature of power spirals, increasing the arm length has minimal effect upon the overall antenna size, as the arms become thinner as they spiral out from the center. Therefore the limiting factor on low frequency spirals is the manufacturing process. If it were possible to accurately manufacture spiral arms down to micrometer thicknesses, the spiral's cutoff frequency would reduce dramatically.

This effect, combined with the frequency independent nature of spiral antennas, can also be used to reduce combination spiral antenna size. Reducing antenna size minimally effects performance parameters except for cutoff frequency, as spiral arm length decreases as size decreases. However, by extending the arms until they reach thicknesses unachievable by the milling, cutoff frequency could be held constant while antenna size is reduced. This would be particularly valuable in portable radar applications.

8.3 Radiation Pattern Measurements

One important parameter that was not accounted for in these tests is radiation pattern. Broadside gain was calculated from the S_{21} measurement, and 90 degrees from broadside was calculated from the cross coupling measurement, however no other angles were characterized. By properly characterizing the overall radiation pattern of the spiral, a better understanding can be achieved of its potential in applications other than ground-penetrating radar arrays.

REFERENCES

[1] S. Azevedo and T. E. McEwan, "Microwave Impulse Radar," *Science and Technology Review,* pp. 17-29, January/February 1996.

[2] D. J. Daniels, "Ground Penetrating Radar," in *Encyclopedia of RF and Microwave Engineering*, John Wiley & Sons, Inc., 2005.

[3] H. G. Schantz, "Dispersion and UWB Antennas," Next-RF, Inc, Huntsville, AL.

[4] A. Dumoulin, J. Matthias, P. McEvoy and M. Ammann, "Performance Evaluation of Antennas for UWB Radar and Positioning Systems," in *Antenna & High Requency Research Centre*, Dublin, 2009.

[5] T. E. McEwan, "Ultra-Wideband Horn Antenna with Abrupt Radiator". US Patent 5,754,144, 19 May 1998.

[6] V. H. Rumsey, "Frequency Independent Antennas," Urbana, Illinois.

[7] M. A. Elmansouri and D. S. Filipovic, "Low-Dispersion Spiral Antennas," *IEEE Transactions on Antennas and Propagation,* vol. 60, no. 12, pp. 5522-5530, December 2012.

[8] T. W. Hertel and G. S. Smith, "On the dispersive properties of the conical spiral antenna and its use for pulsed radiation," *IEEE Transactions on Antennas and Propagation,* vol. 51, no. 7, pp. 1426-1433, 2003.

[9] M. A. Elmansouri and D. S. Filipovic, "Pulse Distortion and Mitigation Thereof in Spiral Antenna-Based UWB Communication Systems," *IEEE Transactions on Antennas and Propagation,* vol. 59, no. 10, pp. 3863-3871, 2011.

[10] Rogers Coporation Microwave Materials Division, "RT/duroid 5880 Glass Microfiber Reinforced Polytetrafluoroethylene Composite," Rogers Corporation, Chandler, AZ, 1999.

[11] "Copper Thickness FAQ," PCB Universe, [Online]. Available: http://www.pcbuniverse.com/pcbu-tech-tips.php?a=4. [Accessed 15 April 2015].

[12] LPKF Laser & Electronics, "LPKF ProtoMat S100," Wilsonville, OR.

[13] National Instruments, "EM: AXIEM," NI, [Online]. Available: https://awrcorp.com/download/faq/english/docs/Simulation/axiem.html. [Accessed 11 April 2015].

[14] S. W. Qu, C. L. Ruan, B. Z. Wang and Q. Xue, "Planar bow-tie antenna embedded in circular aperture within conductive frame," *IEEE Antennas and Wireless Propagation Letters,* vol. 5, no. 1, pp. 399-401, 2006.

[15] Q. Liu, C. -L. Ruan, L. Peng and W. -X. Wu, "A Novel Compact Archimedean Spiral Antenna with Gap-Loading," *Progress in Electromagnetics Research Letters,* vol. 3, pp. 169-177, 2008.

[16] P. C. Werntz and W. L. Stutzman, "Design, Analysis, and Construction Of An Archimedean Spiral Antenna and Feed

Structure," in *Southeastcon*, 1989.

[17] B. Wang and A. Chen, *Design of an Archimedean Spiral Antenna,* 2008.

[18] J. D. Dyson, "The Characteristics and Design of the Conical Log-Spiral Antenna," *IEEE Transactions on Antennas and Propagation,* pp. 488-499, 1965.

[19] Y. Li, Z. Xie and Q. Chu, "A Novel Time-Domain UWB Antenna," in *ICCS*, 2008.

[20] C. G. Hynes, "Evaluation of Methods for Estimating the Cross-Correlation Coefficient Between Closely Spaced Diversity Antennas," University of British Columbia, 2007.

[21] M. A. Elmansouri and D. S. Filipovic, "Characterization of Pulse Distortion and Dispersion of Spiral Antennas," 2010.

[22] R. Hartley, "Microstrip Substrate Equations," RFCafe, [Online]. Available: http://www.rfcafe.com/references/electrical/microstrip-eq.htm. [Accessed 26 March 2015].

APPENDICES

Appendix A

To calculate pulse fidelity values for Table 3, the time domain response of each antenna was measured under four different pulse excitations. Equation 5 was then used to calculate the maximum cross-correlation between input and output values and normalize results to values between 0 (perfectly uncorrelated) and 1 (perfectly correlated). Time domain waveforms of each input pulse and their resulting responses are shown in Figure 39 through Figure 50.

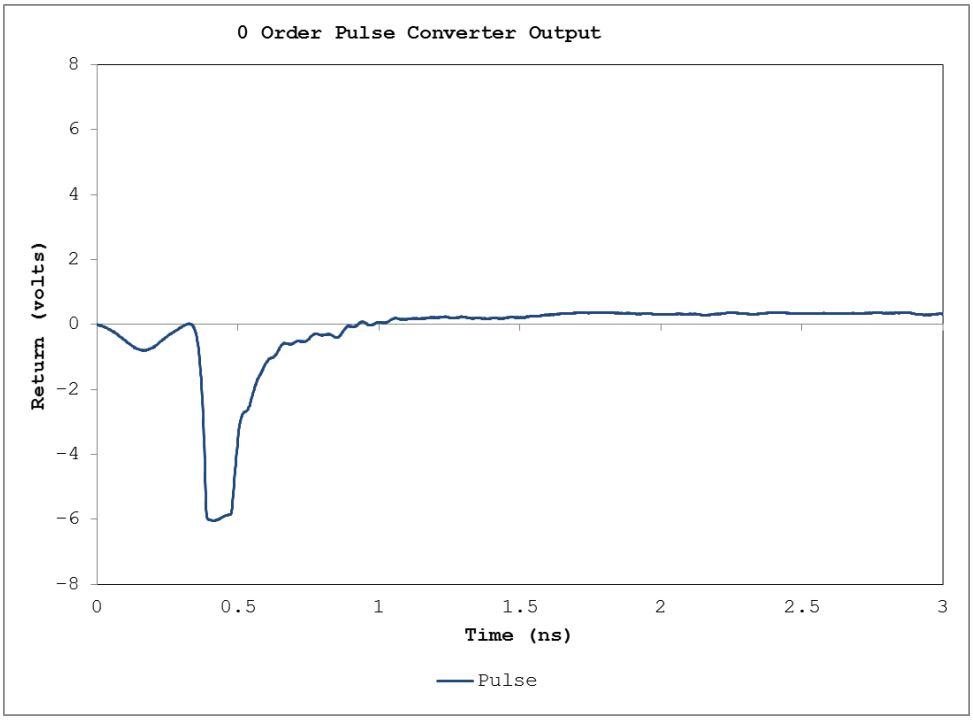

Figure 39: Time domain capture of output pulse from the Pulse Converter configured for a 0 order pulse. Excitation for Figure 40 and Figure 41 responses.

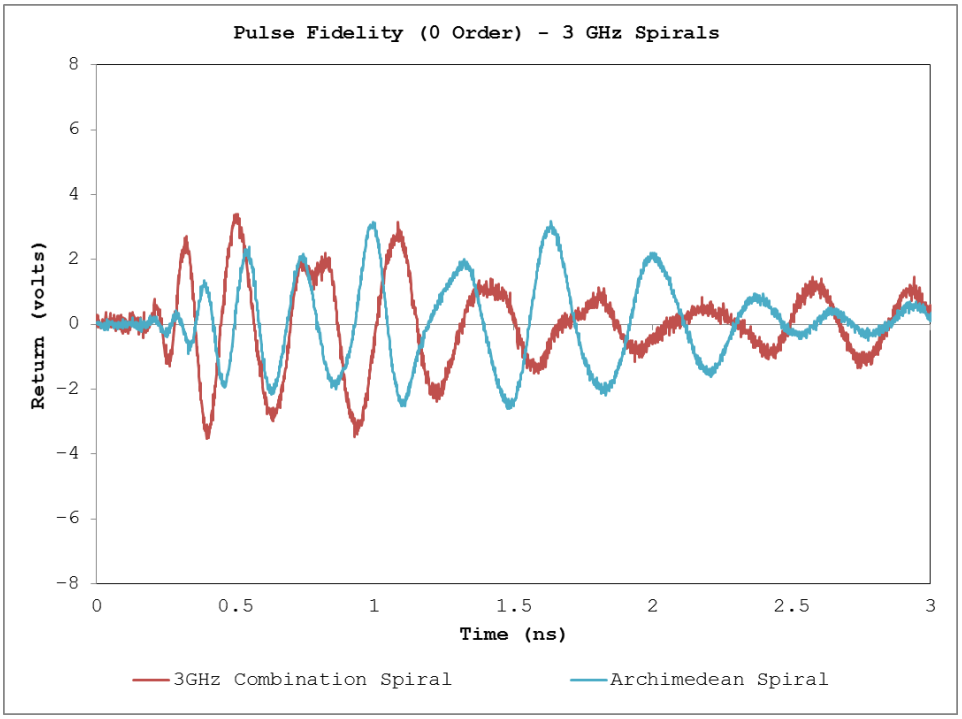

Figure 40: Comparison between simple Archimedean and combined spiral designs.

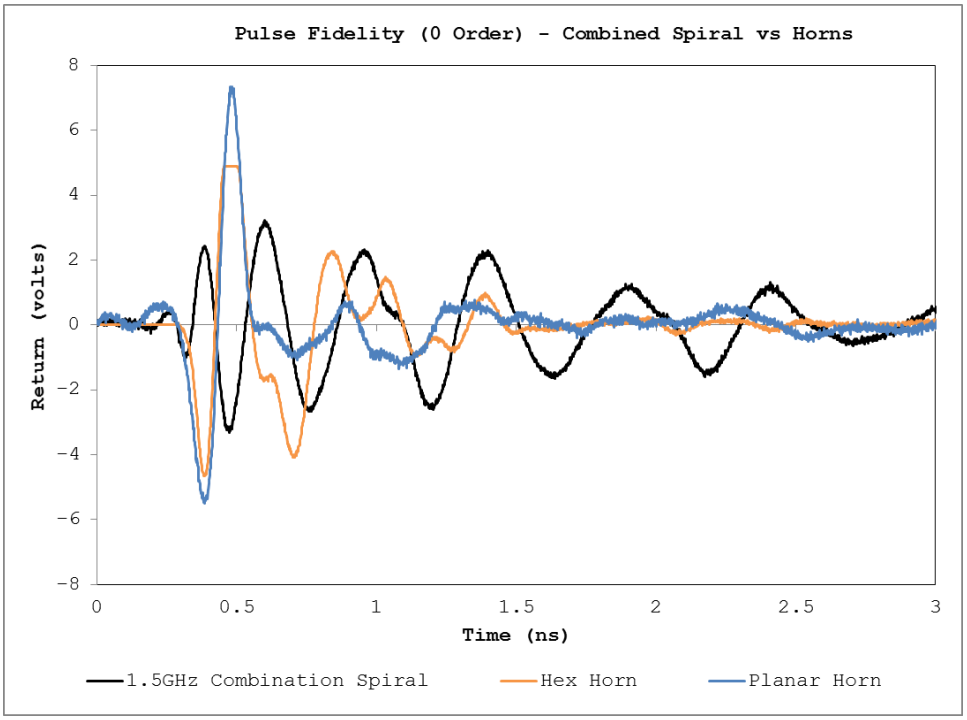

Figure 41: Comparison between the 1.5 GHz combined spiral and both horn antenna designs.

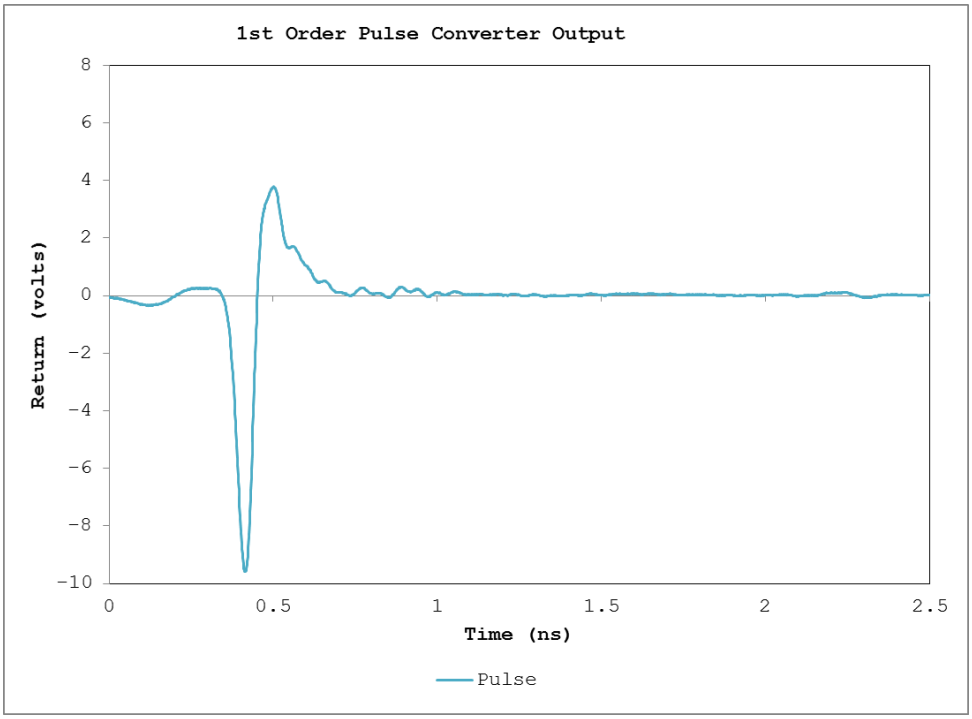

Figure 42: Time domain capture of output pulse from the Pulse Converter configured for a 0 order pulse. Excitation for Figure 43 and Figure 44 responses.

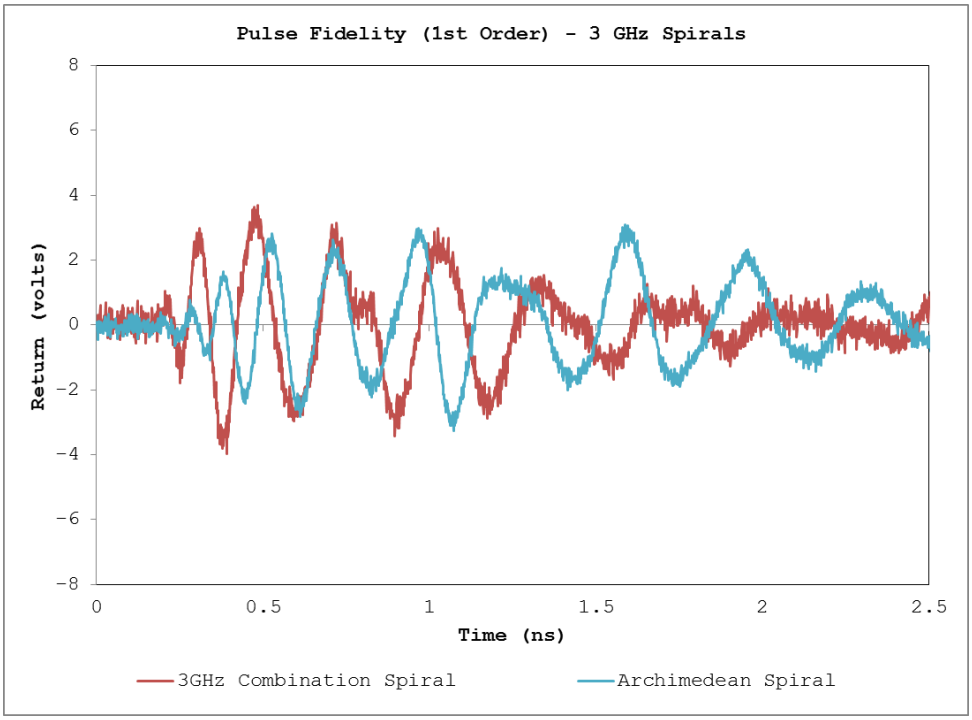

Figure 43: Comparison between simple Archimedean and combined spiral designs.

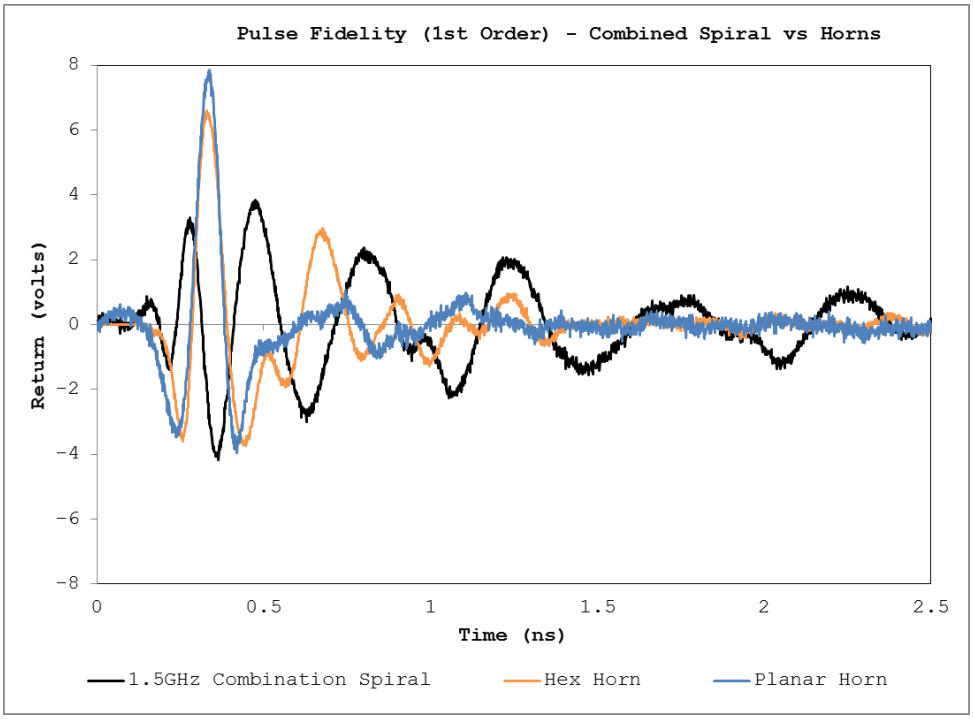

Figure 44: Comparison between the 1.5 GHz combined spiral and both horn antenna designs.

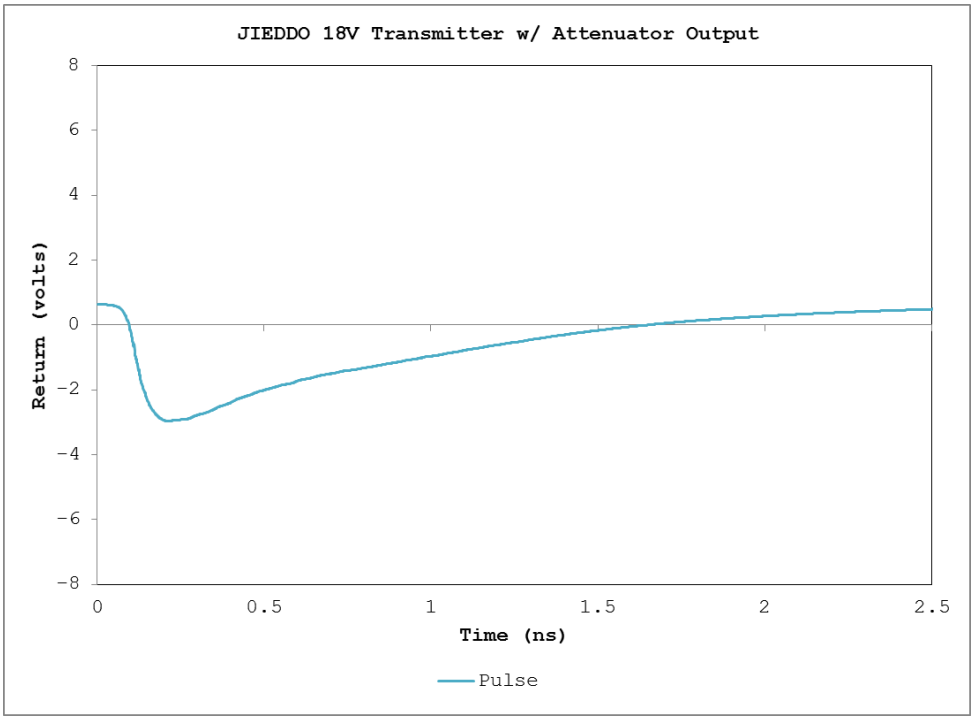

Figure 45: Time domain capture of output pulse from the Pulse Converter configured for a 0 order pulse. Excitation for Figure 46 and Figure 47 responses.

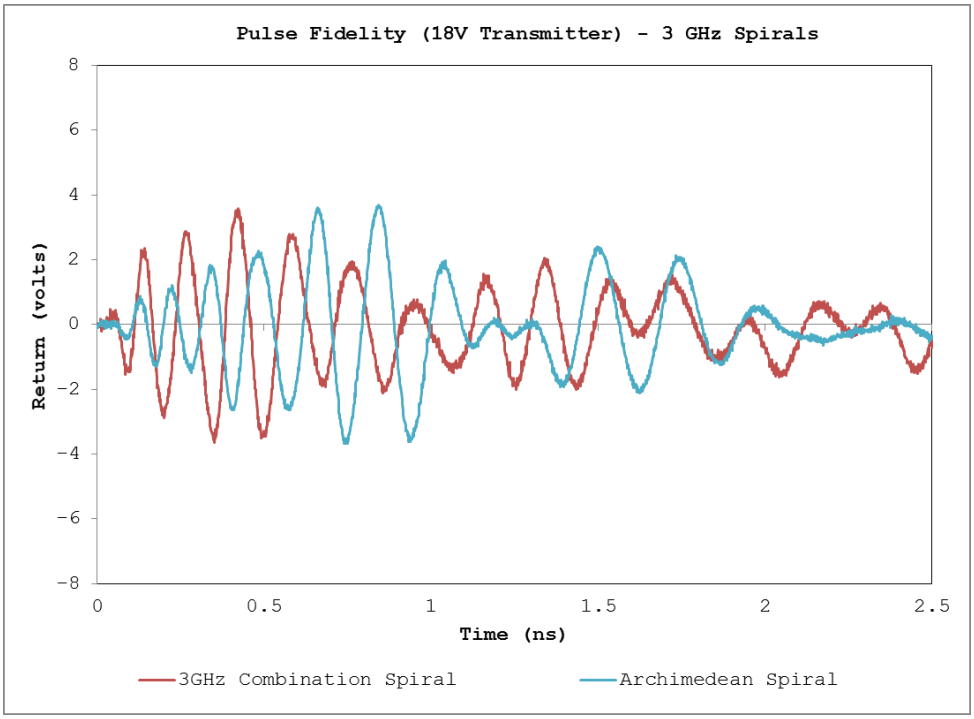

Figure 46: Comparison between simple Archimedean and combined spiral designs.

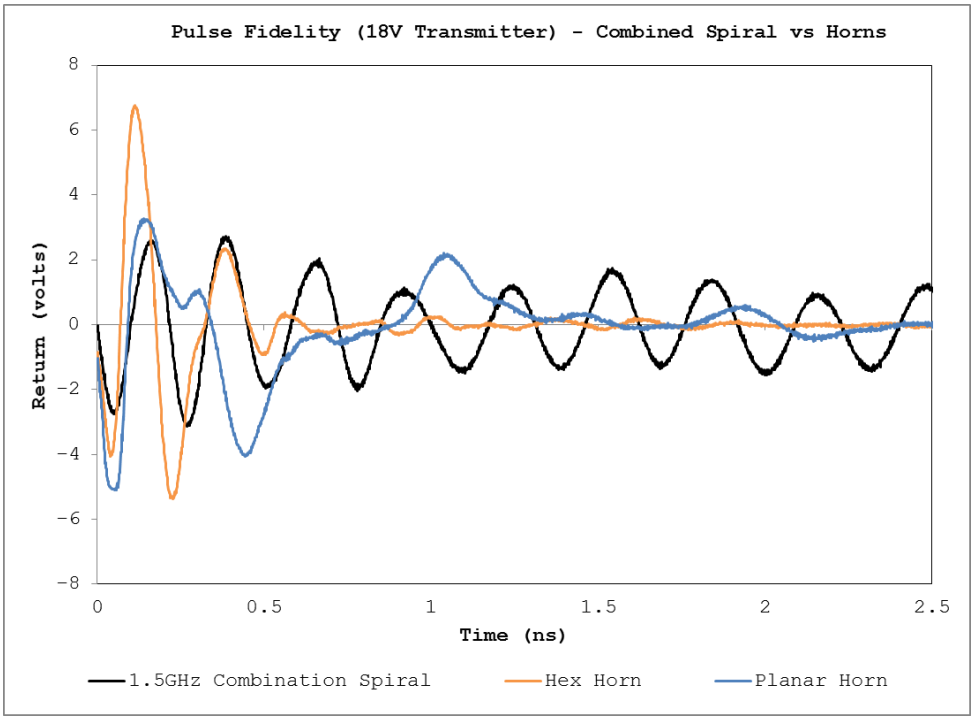

Figure 47: Comparison between the 1.5 GHz combined spiral and both horn antenna designs.

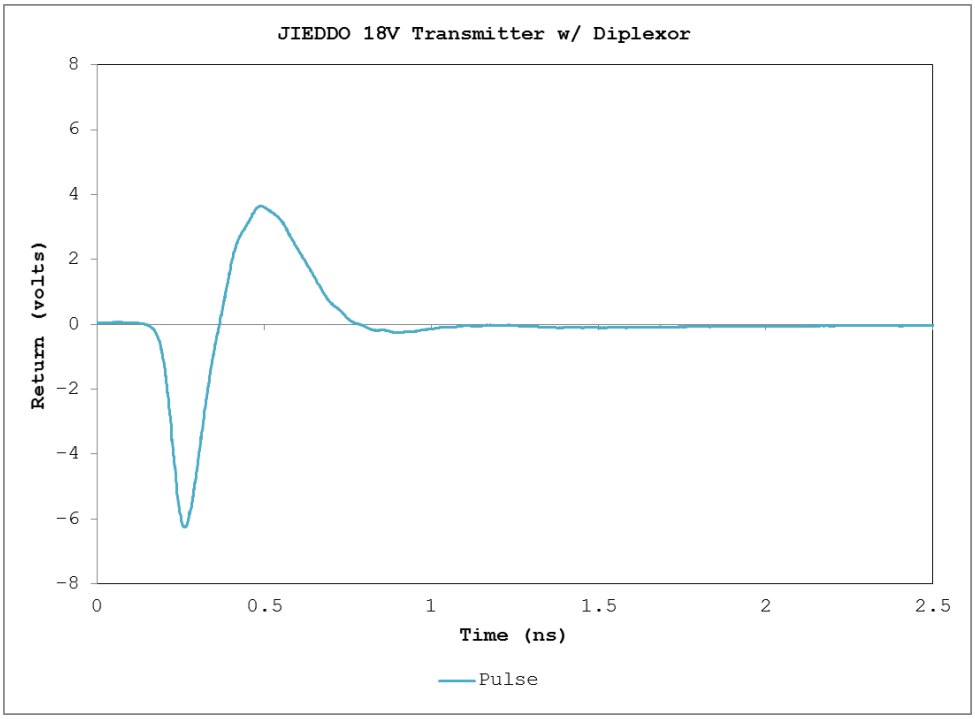

Figure 48: Time domain capture of output pulse from the Pulse Converter configured for a 0 order pulse. Excitation for Figure 49 and Figure 50 responses.

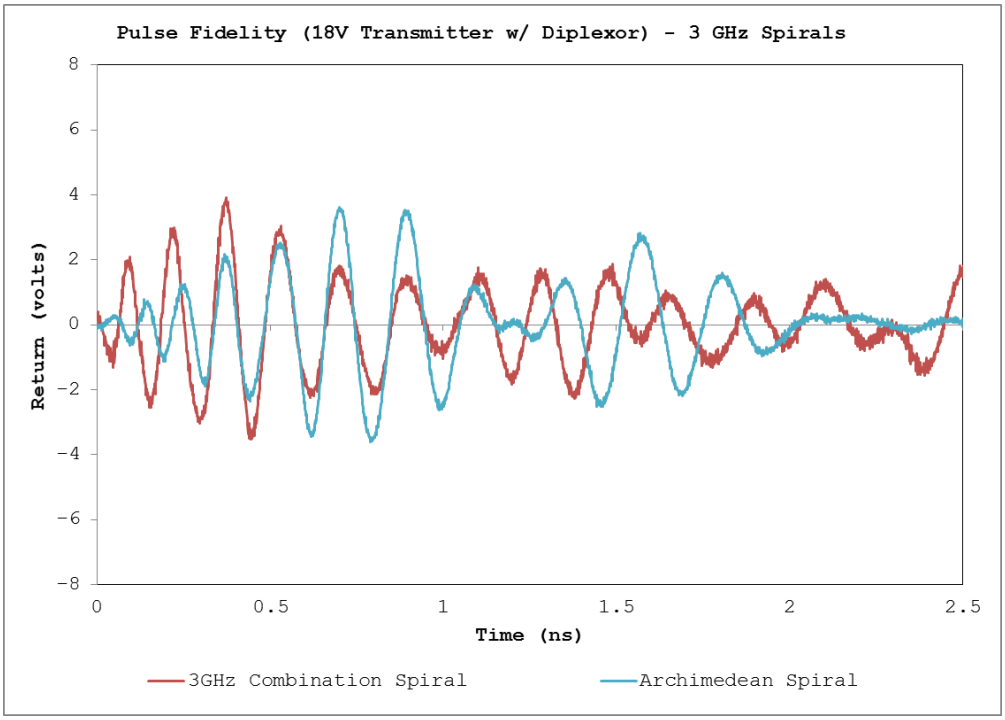

Figure 49: Comparison between simple Archimedean and combined spiral designs.

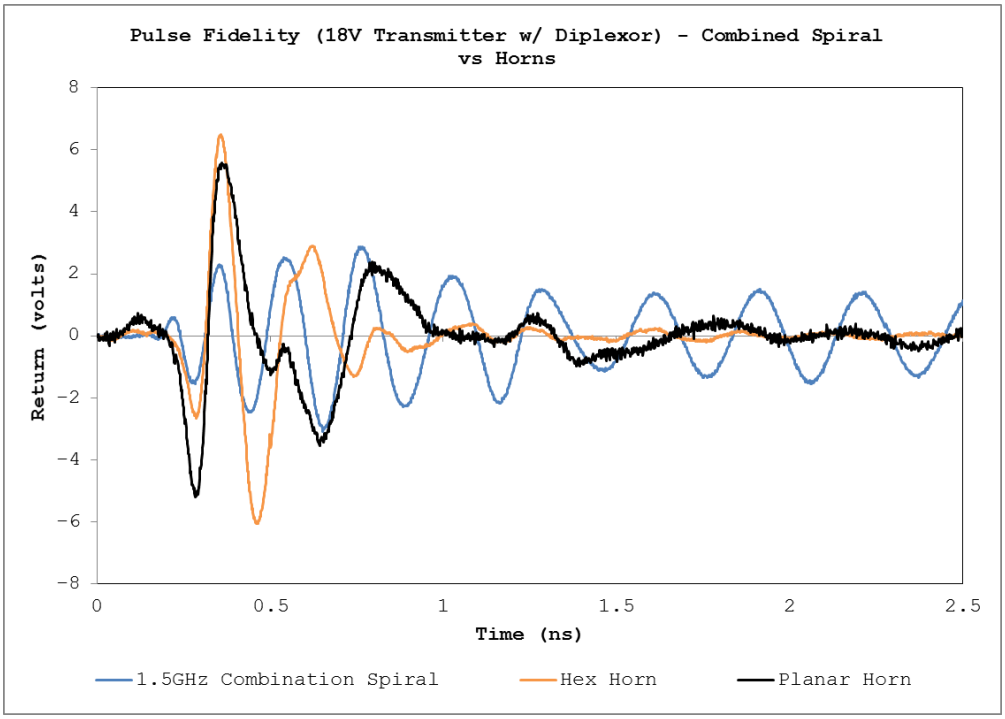

Figure 50: Comparison between the 1.5 GHz combined spiral and both horn antenna designs.